



Flow of a yield-stress fluid past a topographical feature

Edward M. Hinton^{a,*}, Andrew J. Hogg^b

^a School of Mathematics and Statistics, The University of Melbourne, Parkville, VIC 3010, Australia

^b School of Mathematics, University of Bristol, Fry Building, Woodland Road, Bristol, BS8 1UG, United Kingdom

ARTICLE INFO

Keywords:

Bingham
Free-surface flow
Lava flow
Viscoplastic
Topography
Gravity-driven flow

ABSTRACT

Free-surface flows of yield-stress fluids down inclined planes are modelled under the assumptions that they are shallow and sustained by a uniform oncoming stream to determine the steady state that emerges as the flow passes topographic features. In general, the flow may surmount the topography and be deflected around it depending on the thickness of the oncoming flow, the lateral extent and elevation of the mound, the inclination of the plane, and the magnitude of the yield stress relative to the gravitational stress of the flowing layer. Flows deepen upstream of mounds, with amplitude increasing with increasing yield stress. In the absence of a yield stress, flows around isolated mounds exhibit a maximum thickness at a location that is displaced laterally and downstream of the mound due to flow diversion. However, the location of the maximum thickness differs for yield-stress fluids: with increasing yield stress, the flow thickens immediately upstream of the mound and the deflected flux is diminished, leading to a sharp transition in the location of the maximum. Larger amplitude mounds may not be surmounted at all, leading to 'dry zones' downstream into which no fluid flows. It is shown that the steady shape of the dry zone is dependent on the initial condition, because the transient evolution towards it depends upon the plug at its margin, which is not unique. The results are computed by numerical integration of the governing equations and through their asymptotic analysis in various flow regimes to draw out the interplay of the dynamical processes.

1. Introduction

The effects of topography are ubiquitous in gravity-driven geophysical flows including avalanches, mudflows, lahars, lava flows, glaciers and ice sheets, while also playing a key role in coating and film deposition processes [1,2]. These problems have sometimes been modelled as the interaction of Newtonian viscous fluids with topography, which has yielded important insights such as the sensitive dependence of the flow thickness on the steepness of the topography and the very gradual return to constant thickness sheet-flow downstream in three-dimensional geometries [3–7]. However, many of the flows of interest exhibit non-Newtonian behaviour, which has a strong effect on the motion [8–11]. In this article, we analyse the steady, gravitationally-driven, free-surface flow of a yield-stress fluid interacting with various topographic features on an inclined plane, complementing and contrasting with the recent study of the Newtonian analogue of this problem [7].

The importance of topography in directing, splitting and channelling volcanic lava flows has led to great efforts to measure the elevation near volcanoes at high resolutions in order to predict flow routes [12–14]. Significant efforts have also been made to determine the bed elevation underlying ice sheets and the topography for the likely paths of debris flows [15,16]. Hazard assessments are strongly

informed by topographical effects; for example depressions can focus the flow and enhance the likelihood of inundation [17]. Constructed mounds, barriers, and even depressions produced by aerial bombing have been deployed to defend against lava flows and we aim to inform improved design practices [18,19]. There are many numerical tools that determine how lava, fluidised debris and ice sheets flow over a specified and detailed input topography [20,21]. Our approach complements these studies by analysing a model of shallow flow over and around an idealised topographical feature in which we draw out the effects of a yield stress in flowing material. This provides simple generic insights to a wide range of geophysical and industrial applications.

Our analysis builds on much previous research of shallow free-surface flows. The motion of a viscous Newtonian fluid on a smooth inclined plane has been studied in the shallow regime and has provided a useful base for exploring the diversion of such flows around obstacles [22,23]. Hinton et al. [7] showed that isolated mounds divert the viscous flow, which then returns to its unperturbed behaviour further downstream. Shallow viscous films flow over topography that is everywhere downhill but when there is an uphill region, the flow either forms an upstream deep pond to surmount the mound or there is a dry zone in its lee depending on the lateral extent of the mound.

* Corresponding author.

E-mail address: edward.hinton@unimelb.edu.au (E.M. Hinton).

In flows where surface tension plays a key role, dry zones can be sustained even on planar horizontal and inclined surfaces [24,25]. Cylindrical and oblique obstructions to the shallow flow have also been analysed [26–30].

Studies of Newtonian fluids on inclined planes have been extended to treat many different rheological and non-isothermal aspects of environmental flows [10,31,32]. The shallow flow of a viscoplastic fluid over an inclined plane has a velocity profile consisting of an upper region where the velocity gradient is negligible and a lower region with parabolic profile (Fig. 1(a)) [33]. At first sight, it seems that the upper layer is a plug whilst nearer the base the fluid yields owing to gradients of the hydrostatic pressure. However, asymptotic analysis in the lubrication regime reveals that this upper layer is actually a ‘pseudo-plug’ held just above the yield stress and the magnitude of the velocity gradients are negligible but non-zero; the two regions are separated by a ‘fake’ yield surface [34]. Only the leading order velocity profile is needed for analysing the behaviour of the free surface.

The evolution of yield-stress flows on inclined planes arising from vents, extrusions and dam breaks have been well-studied [35]. For example, a finite volume of Bingham fluid released on an inclined plane eventually comes to rest because gravitational forces no longer overcome the yield stress [33]. The final profile is sensitive to the initial condition and subsequent evolution as the regions in which the fluid never yields must be determined [36,37]. We find that the difficulty of selecting the correct late-time profile also arises in the steady flow around topography in the case that there is a dry region (discussed in Section 5.2). Another challenge associated with calculating the steady state is the very slow (algebraic) convergence of transient yield-stress flows to their final shape [38].

The late-time profile of a finite slump of yield-stress fluid on a surface with varying topography was calculated by Balmforth et al. [39]. The role of topography and obstructions on the migration of finite slumps has also been investigated numerically [40]. Other researchers have considered viscoplastic flow in open channels [41] and over substrates such as cylinders and cones, again obtaining various possible late-time profiles [42,43]. In this paper, we analyse the late-time, steady flow around a topographic feature emanating from a constant-flux line source. Our investigation contrasts with previous works by considering the non-stationary, steady flow around the feature rather than the final shape of a fixed volume of fluid. We limit the analysis to a simple Bingham fluid to provide clarity for the effects of a yield stress on the interaction, noting that the analysis of other viscoplastic models would be straightforward extensions. We neglect surface tension, which is unimportant at environmental scales, and inertia on the assumption that viscous and yield-stress processes are dominant, as is the case for many lava, mud and debris flows [44].

The paper is structured as follows. In Section 2, we derive the governing equations and introduce three dimensionless groups that represent the magnitude of the yield stress relative to viscous stresses, and the flow thickness and topography amplitude relative to the lengthscale of the topography. The analysis begins with the case of a topographic feature that is laterally extensive so that the problem is one-dimensional (Section 3). We identify that the flow thickness response to the topography is more exaggerated for fluids with higher yield stresses. An isolated mound (Section 4) leads to both diversion of fluid around the mound and thickening of the flow upstream. For a Newtonian fluid, the former is the much stronger effect but in contrast, the latter plays an increasing role with larger yield stresses. The flow may not surmount an isolated mound with an uphill zone (Section 5) and instead is entirely diverted leading to a dry zone in which there is no fluid. For a yield-stress fluid, the shape of the dry zone is sensitive to the initial conditions that lead to the steady state (Section 5). We discuss applications of our results and make concluding remarks in Section 6.

2. Governing equations

We consider the flow of a Bingham fluid down an inclined plane at an angle β to the horizontal (Fig. 1). The fluid has density ρ and we neglect the effects of inertia (i.e. small Reynolds number). The constitutive law is given by the Bingham model [45]; the fluid is rigid when the yield stress, τ_0 , is not exceeded and the stress is a linear function of the strain rate when the yield stress is exceeded with ‘viscosity’ μ . We orientate the coordinate axes as follows: the \hat{x} axis is directed down-slope, the \hat{y} axis cross-slope and the \hat{z} axis is perpendicular measured from $\hat{z} = 0$ at the topography. The topography is written as a perturbation to the underlying plane of the form $Dm(\hat{x}, \hat{y})$ (with height scale D), where $m \rightarrow 0$ as $\hat{x} \rightarrow \pm\infty$ (see Fig. 1). The flow is supplied by a line-source, located far upstream of the topography, which delivers a constant flux per unit width, Q_0 . We consider the steady flow which develops long after the leading front of the fluid has passed the topography. In the steady state, the flow thickness above the topography is denoted by $\hat{z} = \hat{h}(\hat{x}, \hat{y})$.

We assume that the flow is relatively shallow and apply the lubrication approximation, corresponding to the velocity component in the \hat{z} direction, \hat{w} , being much smaller than that in the \hat{x} and \hat{y} directions (\hat{u}, \hat{v} , respectively), $\hat{w} \ll \hat{u}, \hat{v}$. The pressure is then hydrostatic to leading order. Combined with Bingham’s model this formulation furnishes the well-known velocity profile shown in Fig. 1 [34]. There is a ‘pseudo-plug’ in the upper region where the yield stress is just exceeded and the velocity gradients vanish to leading order. In the lower region, the yielded fluid has a parabolic velocity profile to leading order [34].

Far upstream of the topography, the steady flow has constant thickness, H_∞ , and the flux balance in the \hat{x} direction is given by [33,34]

$$Q_0 = \frac{\rho g \sin \beta}{6\mu} (H_\infty - H_Y)^2 (2H_\infty + H_Y), \quad (1)$$

where

$$H_Y = \frac{\tau_0}{\rho g \sin \beta} \quad (2)$$

is the constant thickness of the ‘pseudo-plug’ far upstream and $H_Y < H_\infty$ by assumption (see Fig. 1). Eq. (1) may be used to obtain the thickness H_∞ given the flux, Q_0 and the yield stress, τ_0 .

To non-dimensionalise the problem, we scale flow thicknesses with H_∞ and lengths with the streamwise lengthscale of the topography, L ,

$$(z, h) = (\hat{z}, \hat{h})/H_\infty, \quad (x, y) = (\hat{x}, \hat{y})/L, \quad m(x, y) = m(\hat{x}/L, \hat{y}/L). \quad (3)$$

We scale the flux per unit width with $\rho g H_\infty^3 \sin \beta / (3\mu)$, which is the far-upstream flux per unit width for a constant thickness Newtonian flow. The Bingham number is

$$B = \frac{\tau_0}{\rho g H_\infty \sin \beta}, \quad (4)$$

which represents the magnitude of the yield stress relative to downslope gravitational stress. Alternatively we can write $B = H_Y/H_\infty$, which is the ratio of the plug thickness to the flow thickness far upstream. We note that H_∞ is an increasing function of the yield stress τ_0 (see Eq. (1)) and by construction, $0 \leq B < 1$. Far upstream, the dimensionless flow thickness is unity, the yield surface is at $z = 1 - B$ and the dimensionless flux is $(1 - B)^2(1 + B/2)$, which is plotted in Fig. 1(b); it is a monotonically decreasing function of B in $[0, 1)$. Under this non-dimensionalisation, material that is flowing but with relatively high yield stress corresponds to $(1 - B) \ll 1$.

Upon incorporating the topography in the hydrostatic pressure, the dimensionless flux is given by [39]

$$q = \frac{1}{2} Y^2 (3h - Y) \left(1 - \mathcal{F} \frac{\partial h}{\partial x} - \mathcal{M} \frac{\partial m}{\partial x}, -\mathcal{F} \frac{\partial h}{\partial y} - \mathcal{M} \frac{\partial m}{\partial y} \right), \quad (5)$$

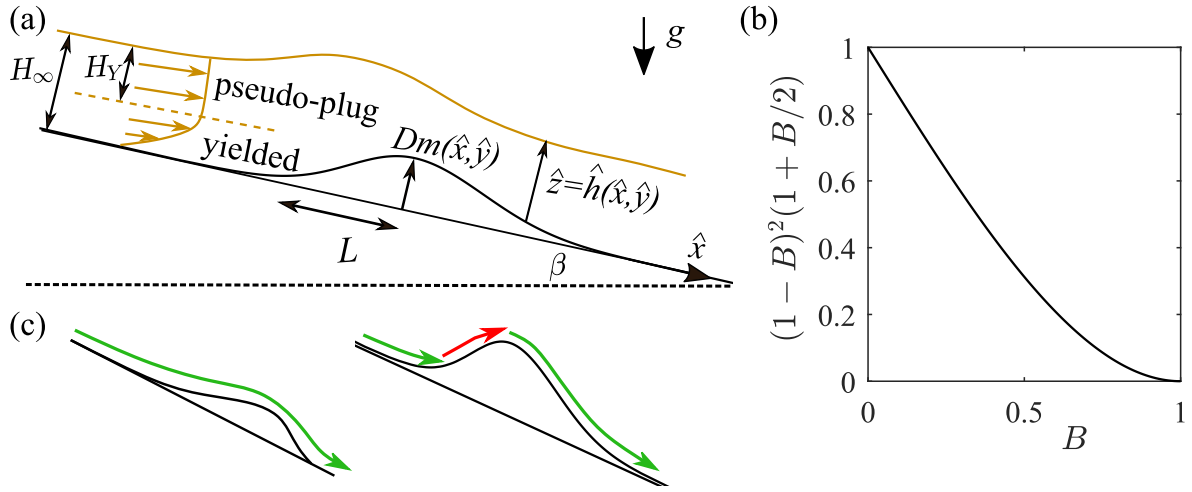


Fig. 1. (a) Schematic of the steady flow over topography. The \hat{y} axis is into the page. (b) The far-upstream dimensionless flux, $(1-B)^2(1+B/2)$ as a function of the dimensionless yield stress, B . (c) ‘Downhill’ topography (green arrows) and ‘uphill’ topography (red arrow).

where

$$Y = \max\left(0, h - \frac{B}{\sqrt{(1-Fh_x - \mathcal{M}m_x)^2 + (Fh_y + \mathcal{M}m_y)^2}}\right), \quad (6)$$

represents the location of the ‘fake’ yield surface and the subscripts $_x$ and $_y$ denote $\partial/\partial x$ and $\partial/\partial y$, respectively. We have introduced the following two dimensionless parameters, [7]

$$F = H_\infty/(L \tan \beta), \quad \mathcal{M} = D/(L \tan \beta), \quad (7)$$

which represent the flow thickness and amplitude of the topography relative to the extent of the topography and the gradient of the underlying plane, respectively. In the steady state, mass conservation is given by

$$\nabla \cdot \mathbf{q} = 0. \quad (8)$$

We restrict our attention to topographic features for which $m(x, y) \rightarrow 0$ as $x \rightarrow \pm\infty$. In this case, the flow returns to its unperturbed state far upstream and downstream of the topography, which imposes the following boundary condition

$$h \rightarrow 1 \quad \text{as } x \rightarrow \pm\infty. \quad (9)$$

To illustrate the key aspects of the interaction with the topography, we consider $m(x, y) = \exp(-x^2)$ in Section 3, which is laterally extensive so that the problem is one-dimensional, and $m(x, y) = \exp(-x^2 - y^2)$ in Section 4, which is an isolated, axisymmetric feature. We note that other topographic profiles could easily be considered as well. With these choices, the topography represents a mound for $\mathcal{M} > 0$ and a depression for $\mathcal{M} < 0$. We also define the topographic elevation as

$$T(x, y) = -x + \mathcal{M}m(x, y), \quad (10)$$

which is analogous to the dimensionless elevation above sea-level (i.e. relative to the dashed horizontal line in Fig. 1(a)). Its dimensional scale is $L \sin \beta$. We note that the free-surface elevation is at $T(x, y) + Fh(x, y)$.

Throughout this paper, we focus on $F \ll 1$ as this regime, where the flow is thin relative to the topography, exhibits many interesting behaviours such as dry zones and ponding. In addition, in this regime the topography has a very strong influence on the flow paths. For relatively thick flows ($F \gg 1$), hydrostatic pressure gradients associated with thickness variations play the dominant role in steering the motion rather than the topographic gradients (and very often the perturbations to the free-surface are negligible).

We solve Eq. (8) numerically and use asymptotic analysis in the regime $F \ll 1$ to identify the dominant features of the flow.

3. Laterally extensive topography

In this section, we analyse steady flow over a laterally extensive topographic feature for which $m(x, y) = m(x)$. The steady problem is one-dimensional, $h = h(x)$. We neglect any instabilities that could cause this film to develop undulations in the transverse direction and even break up into rivulets as may occur in rimming flow inside cylinders [42,46]. We use $m(x) = \exp(-x^2)$. Although this is a simplified geometry, it reveals some key features of the flow over topography, which are important in their own right, and assists in the analysis of an isolated mound in Section 4.

The flux in the downslope direction is constant, which yields the following governing equation for the flow thickness,

$$(1-B)^2(1+B/2) = \frac{1}{2}Y^2(3h-Y) \left(-F \frac{dh}{dx} - \frac{dT}{dx} \right), \quad (11)$$

where

$$Y = h - \frac{B}{(-Fh_x - T_x)}, \quad (12)$$

which is always positive since the flux is a positive constant for $0 \leq B < 1$. The denominator, $-Fh_x - T_x$, is positive for the same reason. We integrate (11) numerically to obtain $h(x)$. The integration is carried out in the negative x direction from $x = +\infty$ ($x = L \gg 1$) owing to a numerical instability that arises when integrating in the positive x direction [7].

We first consider flow over mounds for which there are no ‘uphill’ regions and the topography is everywhere downslope, $-T_x = 1 - \mathcal{M}m_x > 0$ (see Fig. 1(c)). For the Gaussian profile, $m = \exp(-x^2)$, this requires

$$0 < \mathcal{M} < \mathcal{M}_c = \sqrt{e/2} \approx 1.166 \quad (13)$$

For larger mounds with an uphill region ($\mathcal{M} > \mathcal{M}_c$), we anticipate that qualitatively different behaviour occurs as the relatively shallow flow ($F \ll 1$) must thicken significantly to surmount the mound; this situation is analysed in Section 3.1.

The flow thickness, calculated numerically, in the case that $\mathcal{M} = 0.5$ and $F = 0.1$ is shown in Fig. 2(a) for a variety of values of B . For a fixed value of B , there is a larger perturbation to the flow thickness at smaller values of F (see Fig. 2(b)). Fig. 2(a) illustrates that the flow thickens upstream of the mound and thins downstream of the mound prior to returning to its far-field thickness. This effect is magnified with a greater yield stress (larger B). It also appears that in the limit as $B \rightarrow 1$, corresponding to the pseudo-plug occupying almost the entire thickness of the flow, a limiting free surface, which bounds the free

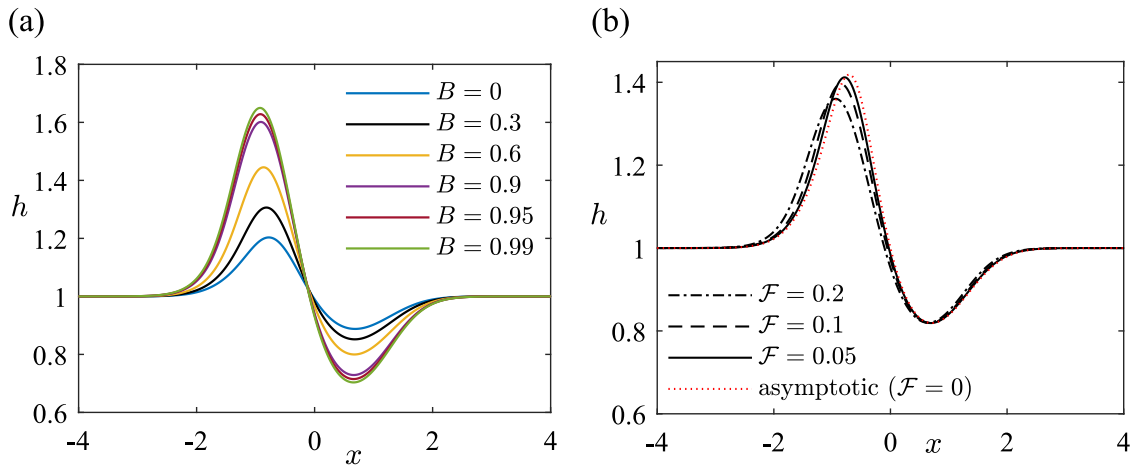


Fig. 2. (a) Steady flow thickness over a mound of amplitude $\mathcal{M} = 0.5$ with $\mathcal{F} = 0.1$ for a variety of values of B . The solutions are calculated numerically. (b) Comparison between the numerical and asymptotic flow thickness in the case $\mathcal{M} = 0.5$ and $B = 0.5$.

surface for $B < 1$ is obtained. We explore these observations through asymptotic analysis.

In the regime $\mathcal{F} \ll 1$, we seek the following expansion for the flow thickness,

$$h = h_0 + \mathcal{F}h_1 + \dots \tag{14}$$

We find that the leading order term, $h_0(x)$, satisfies the following cubic equation

$$(1 - B)^2(1 + B/2) = -\left(h_0 + \frac{B}{T_x}\right)^2 \left(h_0 - \frac{B}{2T_x}\right) T_x, \tag{15}$$

and the second term, $h_1(x)$, satisfies

$$3h_0h_1T_x + \left(h_0^2 - \frac{Bh_0}{2T_x} + \frac{3B^2}{2T_x^2}\right) \frac{dh_0}{dx} = 0 \tag{16}$$

provided that $T_x < 0$ everywhere ('downhill' topography). The leading term, $h_0(x)$, is plotted in Fig. 2(b) for the case $\mathcal{M} = 0.5$ and $B = 0.5$ and shown to capture accurately the numerical solution obtained for three values of \mathcal{F} .

To interpret how the behaviour depends on the yield stress, B , we expand the solution to (15) for small B , which is given by

$$h_0 = (-T_x)^{-1/3} + \frac{B(-T_x)^{-2}}{2} - \frac{B(-T_x)^{-1/3}}{2} + \dots \tag{17}$$

For any value of B , the flow thickness increases when the fluid migrates onto shallower slopes (smaller T_x). This relationship arises because the flux increases with greater flow thickness and decreases with shallower slope. For a constant flux, a shallower slope thus requires a thicker flow. In the case of a Newtonian fluid, the flux is proportional to the thickness cubed and so the thickness is [7]

$$h_0 = (-T_x)^{-1/3}, \tag{18}$$

where $-T_x$ is the inclination. For a Bingham fluid, the dependence of the flow thickness on the slope gradient is much stronger (note the second term in Eq. (17) and see Fig. 2(a)). We interpret this by considering the pressure gradient driving the flow. For thin flows, $\mathcal{F} \ll 1$, the pressure gradient is given by $-T_x$ to leading order. On shallower slopes, the pressure gradient is reduced and so the pseudo-plug occupies a greater proportion of the flow, which reduces the flux. Thus, when a yield-stress fluid migrates onto a shallower slope its thickness increases more than a Newtonian fluid (to maintain a constant flux). The end-members of this behaviour are a Newtonian fluid (18) and a Bingham fluid whose flow is dominated by its large yield stress (B close to 1). The flow thickness for the latter is given by (15)

$$h_0 = (-T_x)^{-1}, \tag{19}$$

which corresponds to $Y \approx 0$ everywhere. The flow thicknesses for $0 \leq B < 1$ in the regime $\mathcal{F} \ll 1$ are thus enclosed in the envelope of the solutions for $B = 0$ and $B \rightarrow 1$ (Fig. 2(a)). The maximum flow thickness in the regime $\mathcal{F} \ll 1$ for $0 \leq B < 1$ may be obtained from the $B \rightarrow 1$ solution; it occurs at $x = -1/\sqrt{2}$ and is given by

$$h_{\max} = (1 - \mathcal{M}/\mathcal{M}_c)^{-1}. \tag{20}$$

The increased sensitivity of the steady flow thickness to the slope gradient at higher yield stresses is a general result that applies to any topographic profile that does not exhibit locally uphill regions.

The present analysis breaks down when $\mathcal{M} > \mathcal{M}_c$, corresponding to a feature with an 'uphill' zone (where $T_x > 0$; see Fig. 1(c)). In this case, the function

$$T_x = -1 + \mathcal{M}m_x = -1 - 2x\mathcal{M}\exp(-x^2) \tag{21}$$

has two zeros and $h_0(x)$ becomes singular at these locations (see the red dashed line in Fig. 3(a)). Hence, different analysis is needed to capture the flow behaviour near the uphill zone.

3.1. Mounds with an uphill region ($\mathcal{M} > \mathcal{M}_c$)

In order for a shallow flow ($\mathcal{F} \ll 1$) that is driven by gravity to surmount uphill topography the flow must deepen; there is no inertia to carry fluid over the hill. We expect that a thick pond of fluid forms upstream of the uphill region (see Fig. 3). The pond has a horizontal free surface to leading order ($T + \mathcal{F}h = \text{constant}$) and so we write

$$h = \mathcal{F}^{-1}h_{-1} + \gamma c_0 + \dots, \quad h_{-1} = -T(x) + c_{-1}, \tag{22}$$

where the magnitude of γ and the two constants, c_{-1} and c_0 are to be determined via matching to the $h \sim 1$ expansion, $h_0(x)$, which is valid away from the pond and given by (15). The solution $h = \mathcal{F}^{-1}h_{-1}$ corresponds to vanishing volume flux and the flux from upstream, $(1 - B)^2(1 + B/2)$ is balanced by lower order terms.

It is useful to define the key points in the topography. We denote the turning points of the topography ($T_x = 0$) by x_0 and x_1 ($x_0 > x_1$) (see Fig. 3(b)). We also define x_2 as the upstream end of the pond and so it satisfies $T(x_2) = T(x_0)$ to leading order. The pond thickness returns to order unity at x_0 and x_2 beyond which the leading order solution, $h_0(x)$ is valid. The full details of the matching at $x = x_0$ of the two asymptotic expansions is given in Appendix A. We find that

$$c_{-1} = T(x_0), \quad c_0 = 2.946, \quad \gamma = \mathcal{F}^{-1/3}[-T_{xx}(x_0)]^{-1/3} B^{2/3}. \tag{23}$$

The pond expansion (22) and $h \sim 1$ expansion (15) are compared to the numerical solution in Fig. 3(a) for the case $\mathcal{M} = 2$, $\mathcal{F} = 0.1$ and $B = 0.5$. The expansion derived here for the pond thickness is valid for any

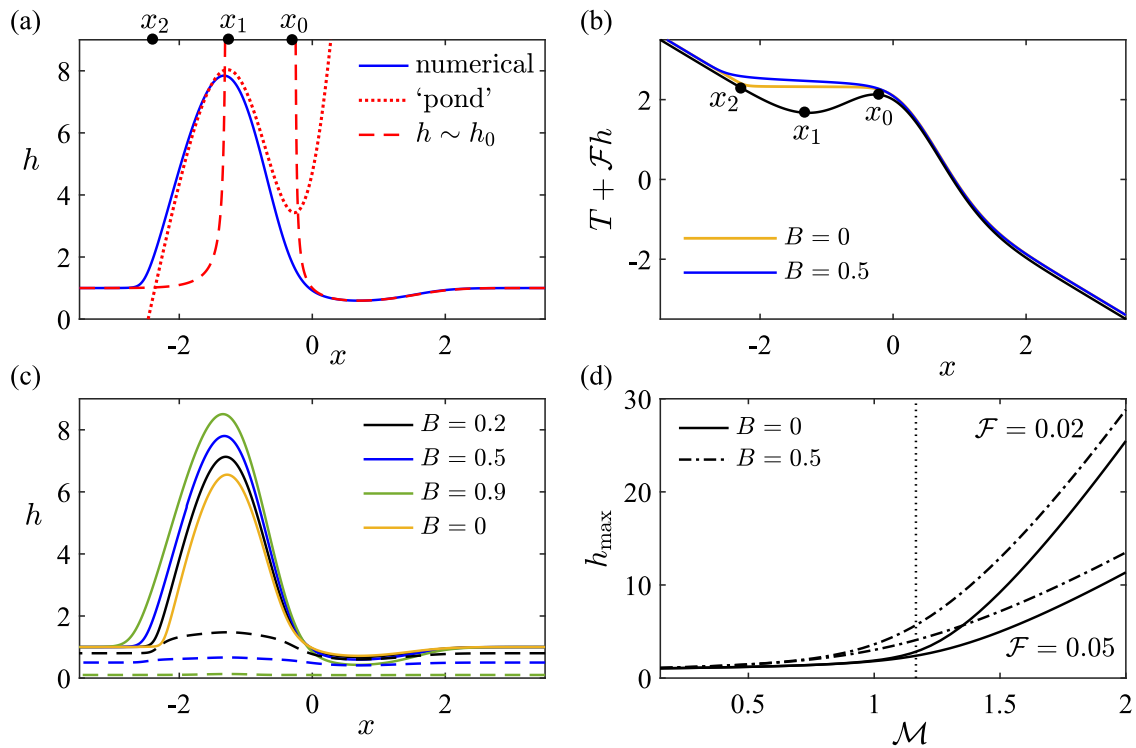


Fig. 3. (a)–(c) ‘Uphill’ mound with $\mathcal{M} = 2$ and $\mathcal{F} = 0.1$. (a) Comparison between the numerical and asymptotic flow thickness for $B = 0.5$. (b) Free surface elevation, $T(x) + \mathcal{F}h(x)$ and the topographical elevation, $T(x)$, (black line). The dots denote the turning points of $T(x)$ (x_0 and x_1) and the upstream end location of the pond (x_2). (c) Steady flow thicknesses, $h(x)$ (continuous lines) and corresponding yield surfaces, $Y(x)$ (dashed lines), for a range of values of B . For $B = 0$, $Y = h$. (d) The maximum flow thickness over a mound. The vertical dashed line represents the critical magnitude, $\mathcal{M} = \mathcal{M}_c$ above which there is an ‘uphill’ zone.

value of B , which is sufficiently large to contribute to the γ term. When $B \ll 1$, however, the second order term in the pond expansion must be adjusted. For $B = 0$, it was shown the second term was proportional to $\gamma \sim \mathcal{F}^{-1/7}$ [7] rather than $\mathcal{F}^{-1/3}$, which arises due to the yield stress effects (23). This difference occurs because for a Newtonian fluid, the pond is matched to the $h \sim 1$ behaviour via considering mass continuity but for a yield-stress fluid, the pond is matched by instead requiring that the fake yield surface is above the base everywhere ($Y > 0$).

Fig. 3(c) shows the flow thickness and yield surface, Y , for flow over a mound with an uphill region ($\mathcal{M} = 2$) for a range of values of B . The yield surface is much smaller than the flow thickness, $Y \ll h$, within the pond and the flow is mostly plugged in this region with yielding only near the base, $z = 0$. The pond thickness is greater for fluids with greater yield stress.

3.2. Maximum flow thickness

The maximum flow thickness, calculated numerically, is compared between the Newtonian and non-Newtonian cases in Fig. 3(d) for two values of \mathcal{F} . For the case of $\mathcal{M} < \mathcal{M}_c$ in which there are no uphill regions, the maximum flow thickness, h_{\max} , for the Newtonian case ($B = 0$) was found to be [7]

$$h_{\max} = (1 - \mathcal{M}/\mathcal{M}_c)^{-1/3}. \tag{24}$$

Whilst for a yield-stress fluid, the maximum flow thickness is given by $h_{\max} = h_0(-1/\sqrt{2})$.

For larger mounds, $\mathcal{M} > \mathcal{M}_c$, the maximum flow thickness occurs asymptotically at $x = x_1$ and is given by [7] and Appendix A,

$$h_{\max}(B = 0) = \mathcal{F}^{-1} [T(x_0) - T(x_1)] + 1.61 \mathcal{F}^{-1/7} [-T_{xx}(x_0)]^{-1/7}, \tag{25}$$

$$h_{\max}(B > 0) = \mathcal{F}^{-1} [T(x_0) - T(x_1)] + 2.95 B^{2/3} \mathcal{F}^{-1/3} [-T_{xx}(x_0)]^{-1/3}, \tag{26}$$

for the Newtonian and yield-stress cases respectively. The expressions suggest that the system is in the Newtonian regime for $B \ll \mathcal{F}^{2/7}$;

a relationship that arises for any topographic feature with an uphill region.

3.3. Depressions ($\mathcal{M} < 0$)

We briefly discuss the flow behaviour in the case of a laterally-extensive depression corresponding to $\mathcal{M} < 0$. The flow thickens on shallower inclines and thins on steeper inclines. The location of the steeper and shallower inclinations are reversed for a depression from the case of a mound. The leading order thickness, h_0 , is simply a reflection ($x \rightarrow -x$) of the case of $\mathcal{M} > 0$ since $T_x(x; \mathcal{M}) = T_x(-x; -\mathcal{M})$.

For depressions with larger amplitude ($|\mathcal{M}| > \mathcal{M}_c$), a pond forms in order for the flow to surmount the uphill portion of the depression. The solution may be obtained in an identical manner to a mound (for both the first and second order terms in the pond expansion; (15) and (16)), noting that the matching location is translated downstream ($x_0 > 0$). An example with $\mathcal{F} = 0.1$, $B = 0.5$ and $\mathcal{M} = -2$ is shown in Fig. 4. The pond solution we have obtained applies to any laterally extensive topography with an uphill region.

4. Isolated topography

We analyse the interaction with an isolated topographic feature, centred at the origin. For ease of exposition, we focus on an axisymmetric Gaussian mound with elevation given by

$$T = -x + \mathcal{M}m(x, y), \quad m(x, y) = \exp(-x^2 - y^2). \tag{27}$$

However, we note that the analysis and results may be applied to a wide range of isolated topographic features.

The steady flow thickness over such a mound, with amplitude $\mathcal{M} = 0.5$ and flow parameter $\mathcal{F} = 0.1$, is shown in Fig. 5(a) for $B = 0$ and in Fig. 5(b) for $B = 0.5$ (calculated numerically; details of the method are given in Appendix B). The ‘fake’ yield surface, $Y(x, y)$ is shown in Fig. 5(c) for $B = 0.5$. We also include the flow thickness in the

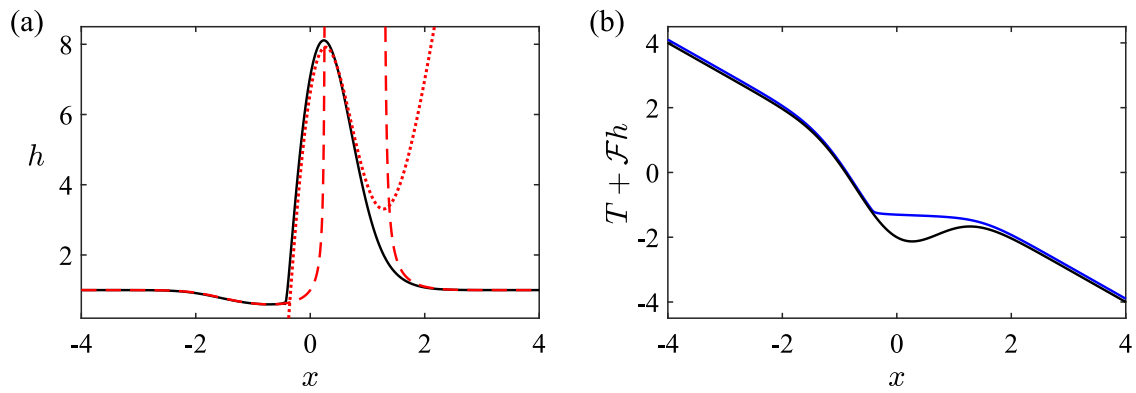


Fig. 4. (a) The flow thickness in the case of a depression with an uphill region ($\mathcal{M} = -2$) with $\mathcal{F} = 0.1$ and $B = 0.5$. The numerical solution is plotted as a continuous line, the pond as a dotted line and the $h \sim 1$ expansion as a dashed line. (b) The elevation of the free-surface (blue line) and the topography (black line).

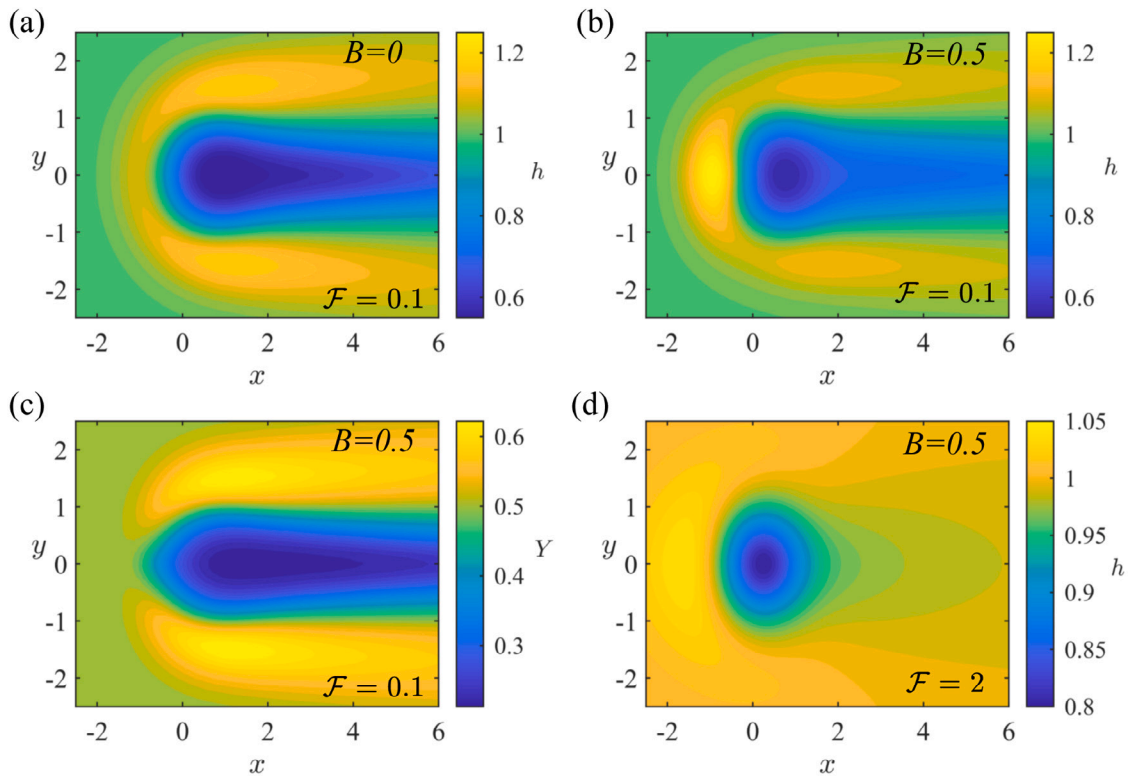


Fig. 5. Steady flow over an isolated mound with $\mathcal{M} = 0.5$. (a) Flow thickness, $h(x, y)$, for $B = 0$ and $\mathcal{F} = 0.1$. (b) Flow thickness for $B = 0.5$ and $\mathcal{F} = 0.1$ (same colour scale as (a)). (c) The plug height, $Y(x, y)$ for $B = 0.5$ and $\mathcal{F} = 0.1$. (d) Flow thickness for a relatively thicker flow ($\mathcal{F} = 2$), with $B = 0.5$.

case that $\mathcal{F} = 2$ in Fig. 5(d). When \mathcal{F} is not small, the free surface is approximately parallel to the underlying plane and the flow thickness adjusts accordingly (i.e. it is thinner over the mound). We focus on the relatively long and wide mound (or equivalently, relatively thin flow) regime, $\mathcal{F} \ll 1$, as in Section 3.

Fig. 5 indicates that generally the flow thickens upstream and to the sides of the mound and is diminished in the lee of the mound. In the case that $B = 0$, the flux is proportional to h^3 , whilst for $B > 0$, the flux is proportional to $Y^2(3h - Y)/2$. In the regime $\mathcal{F} \ll 1$, the flux direction is approximately given by the steepest descent of the topography (as described below). These two observations imply that the variation in the yield surface, Y for $B = 0.5$ is somewhat similar to the flow thickness in the Newtonian case, $B = 0$ (compare Fig. 5(a) and Fig. 5(c)).

The maximum flow thickness occurs upstream of the mound when there is a sufficient yield stress e.g. $B = 0.5$, whereas in the absence of a yield stress ($B = 0$), it occurs cross-stream (see Fig. 5(a) and

Fig. 5(b)). In the case of a significant yield stress, there is less diversion of fluid around the mound, relative to a Newtonian fluid. We explore these observations through asymptotic analysis below. As with laterally extensive mounds (Section 3), the case of an isolated mound with an uphill region is qualitatively different to the present analysis for $\mathcal{M} < \mathcal{M}_c$ and is described in Section 5.

4.1. Asymptotic analysis for a mound ($\mathcal{F} \ll 1$)

For small \mathcal{F} and a mound with no uphill region, we seek an $h \sim 1$ expansion as before,

$$h = h_0 + \mathcal{F}h_1 + \dots \tag{28}$$

To leading order, the ‘fake’ yield surface is at

$$Y = h_0 - \frac{B}{|\nabla T|}. \tag{29}$$

The leading order terms in the governing Eq. (8) are

$$-\frac{\partial T}{\partial x} \frac{\partial \mathcal{P}}{\partial x} - \frac{\partial T}{\partial y} \frac{\partial \mathcal{P}}{\partial y} = \mathcal{P} \nabla^2 T, \quad (30)$$

where

$$\mathcal{P} = \frac{[h_0 - B/|\nabla T|]^2 [h_0 + B/(2|\nabla T|)]}{(1-B)^2(1+B/2)}, \quad (31)$$

and we have the boundary condition $\mathcal{P} \rightarrow 1$ in the far-field, as $x^2 + y^2 \rightarrow \infty$. Since B does not appear in (30) or in the far-field boundary condition, we conclude that $\mathcal{P}(x, y)$ is independent of B . It provides a universal profile from which the thicknesses h_0 may be obtained for different B via inverting Eq. (31). For $\mathcal{F} \ll 1$, the flux at any point relative to the far upstream flux is $-\mathcal{P}\nabla T$, and (30) is simply a statement that $\nabla \cdot (\mathcal{P}\nabla T) = 0$. Indeed, $\mathcal{P}(x, y)$ is proportional to the magnitude of the flux at (x, y) relative to the far upstream flux, $(1-B)^2(1+B/2)$.

We obtain $\mathcal{P}(x, y)$ by applying the method of characteristics,

$$\frac{dx}{d\tau} = -\frac{\partial T}{\partial x}, \quad \frac{dy}{d\tau} = -\frac{\partial T}{\partial y}, \quad \frac{d \log(\mathcal{P})}{d\tau} = \nabla^2 T, \quad (32)$$

where τ parameterises the characteristic curves. We note that this solution method requires $\partial T/\partial x < 0$ everywhere (i.e. downhill).¹

The characteristic projections in the (x, y) plane are shown as continuous red lines in Fig. 6(a) for the case $\mathcal{M} = 0.5$. They follow the steepest descent of the topography and thus represent the flow paths. The relative flux, \mathcal{P} , is also shown in Fig. 6(a) by the colourmap. We note that $\nabla^2 T = 4\mathcal{M}(r^2 - 1)e^{-r^2}$, which is positive for $r > 1$ and greatest at $r = \sqrt{2}$. The two circles $r = 1$ and $r = \sqrt{2}$ are shown as dashed lines in Fig. 6(a) demonstrating that the maximum value of \mathcal{P} occurs on characteristics that pass near these circles. Within the unit circle, the value of \mathcal{P} decreases along characteristics, which is associated with the diversion of flux around the mound; see also equation (32)(c). The flow thickness decreases when characteristics diverge and increases when characteristics converge owing to the flux accumulating.

With the solution $\mathcal{P}(x, y)$ in hand for a given topography, we may invert (31) to obtain a unique solution for h_0 for any B (shown in Fig. 6(b)–(g)). The predicted flow thickness along the centreline, $h_0(x, 0)$ is plotted in Fig. 7(a). As $x \rightarrow \infty$, the relative flux, $\mathcal{P}(x, y) \rightarrow \mathcal{P}_\infty(y)$. The far downstream thickness, $h(x, y) \rightarrow h_\infty(y)$ as $x \rightarrow \infty$, is given by the solution to

$$\mathcal{P}_\infty(y) = \frac{[h_\infty(y) - B]^2 [h_\infty(y) + B/2]}{(1-B)^2(1+B/2)}, \quad (33)$$

since $|\nabla T| = 1$ far downstream to leading order. Moreover, the magnitude of the downstream flux, scaled by its upstream value, is given by $\mathcal{P}_\infty(y)$. The predicted downstream flow thickness $h_\infty(y)$ is plotted in Fig. 7(b).

Figs. 6 and 7, demonstrate that there is a rich dependence of the flow structure on the yield stress in this asymptotic regime. First, it can be observed that the increase in flow thickness just upstream of the mound is stronger for larger values of B (see Fig. 6(b)–(g)). This behaviour was also shown for a laterally extensive mound (Section 3) and is associated with the greater response of a yield-stress fluid to a change in slope. However, unlike a laterally extensive mound, the isolated mound also diverts the flow cross-stream. For a Newtonian fluid, this leads to the maximum flow thickness occurring cross-stream and downstream of the isolated mound (Fig. 6). Figs. 6 and 7 illustrate that for increasing values of B , the downstream flow thickness $h_\infty(y)$ is flattened. In particular, for B close to 1, $h_\infty(y) = 1 + \mathcal{O}(1-B)$ (from

¹ The behaviour for an isolated depression (with no uphill regions; $-\mathcal{M}_c < \mathcal{M} < 0$) may simply be obtained by reflecting the behaviour for a mound ($\mathcal{M} > 0$), as in the case of a laterally-extensive feature. This is because the asymptotic description for h_0 is invariant under the transformation $\mathcal{M} \rightarrow -\mathcal{M}$ and $x \rightarrow -x$.

(33)). This behaviour may be rationalised as follows. We recall that the relative flux, \mathcal{P} is independent of B . The different behaviours arise because for increasing values of B , the absolute flux, $(1-B)^2(1+B/2)$ is smaller and so less fluid is actually diverted, leading to a reduced perturbation to the flow thickness far downstream. In summary, a yield stress leads to the surprising outcome of an increased thickness perturbation upstream of the mound but a decreased thickness perturbation cross-stream and downstream.

We next analyse the controls on the location of the maximum flow thickness. First, for a Newtonian fluid ($B = 0$), we note that $\mathcal{P} = h_0^3$ and the maximum value of h_0 occurs at the same place as for \mathcal{P} , which is far downstream ($x \rightarrow \infty$) and cross stream (c.f. Fig. 5(a) and Fig. 6(a)). This result follows from the leading order expansion for the flow thickness (28), which becomes non-asymptotic far downstream where weak cross-stream gradients become no longer negligible. These effects modify the fluid thicknesses somewhat: see, for example, the small discrepancy between the predicted and simulated maximum thickness when $B \ll 1$ for $\mathcal{F} = 0.03$ (Fig. 8(a)). We reinstate this cross-stream diffusion in Section 4.3 with the consequence that the maximum thickness is found at some finite distance downstream of the topography and at some lateral offset from the $y = 0$ symmetry axis (see Fig. 5(a)).

We also note that the point $(x, y) = (-1, 0)$ is a saddle point of $\mathcal{P}(x, y)$ for any $\mathcal{M} \in (0, \mathcal{M}_c)$ and hence it is also a saddle point of h_0 for a Newtonian fluid ($B = 0$). This may be observed from (32): $d \log(\mathcal{P})/dy = 2y$ at $x = -1$, so $\log(\mathcal{P}) \sim y^2 + \text{const}$ near $y = 0$. Although $(x, y) = (-1, 0)$ is a saddle point of $\mathcal{P}(x, y)$, it may not be a saddle point of h_0 for $B > 0$. At the extremum, $(-1, 0)$ we use (31) to write

$$3h_0 \left(h_0 - \frac{B}{|\nabla T|} \right) \frac{\partial^2 h_0}{\partial y^2} = (1-B)^2(1+B/2) \frac{\partial^2 \mathcal{P}}{\partial y^2} - \frac{3B}{2} \frac{T_x T_{xy} + T_{yy}^2}{T_x^2} \left(h_0^2 - \frac{B^2}{T_x^2} \right). \quad (34)$$

Hence for larger values of the yield stress, the second term on the right-hand side dominates the first and $\partial^2 h_0/\partial y^2$ changes sign so that $(x, y) = (-1, 0)$ becomes a local maximum. For sufficiently large B , the thickness at $(-1, 0)$ is also the global maximum. There is a qualitative change in the behaviour of the maximum flow thickness at a critical value, $B = B_c$. This is demonstrated in Fig. 8(a), where the upstream maximum is plotted as a dashed line, the downstream maximum as a dotted line and the global maximum as a continuous line. For $B < B_c$, the maximum occurs cross-stream and downstream of the mound; it also decreases in magnitude with B . However, for $B > B_c$, the maximum occurs directly upstream of the mound and its magnitude is an increasing function of B . The critical value at which the maximum changes location, $B = B_c(\mathcal{M})$ is shown as a function of \mathcal{M} in Fig. 8(b).

4.2. Large yield stresses ($|1-B| \ll 1$)

The effect of a yield stress on the flow can be further interpreted by analysing the limiting regime of a very large yield stress (B close to 1). For a laterally extensive mound (Section 3), this regime provided an end-member of the behaviour for $0 < B < 1$. For an isolated mound, with $\mathcal{F} \ll 1$ and $B \approx 1$, the fake yield surface is at $Y = 0$ to leading order, which furnishes the leading order expression

$$h_0 = \frac{1}{|\nabla T|} \quad (35)$$

and this satisfies the boundary condition that h_0 returns to 1 far away from the mound. Eq. (35) may also be obtained by taking the limit $B \rightarrow 1$ in the expression for \mathcal{P} (31). This solution provides an envelope of the flow thickness for $0 \leq B < 1$ (an upper bound on the upstream perturbation and a lower bound on the downstream perturbation; see the dashed lines in Fig. 7). The flow thickness according to (35) corresponds to zero diversion of flux around the mound providing the limiting case of the discussion above. Indeed, along the centreline, the

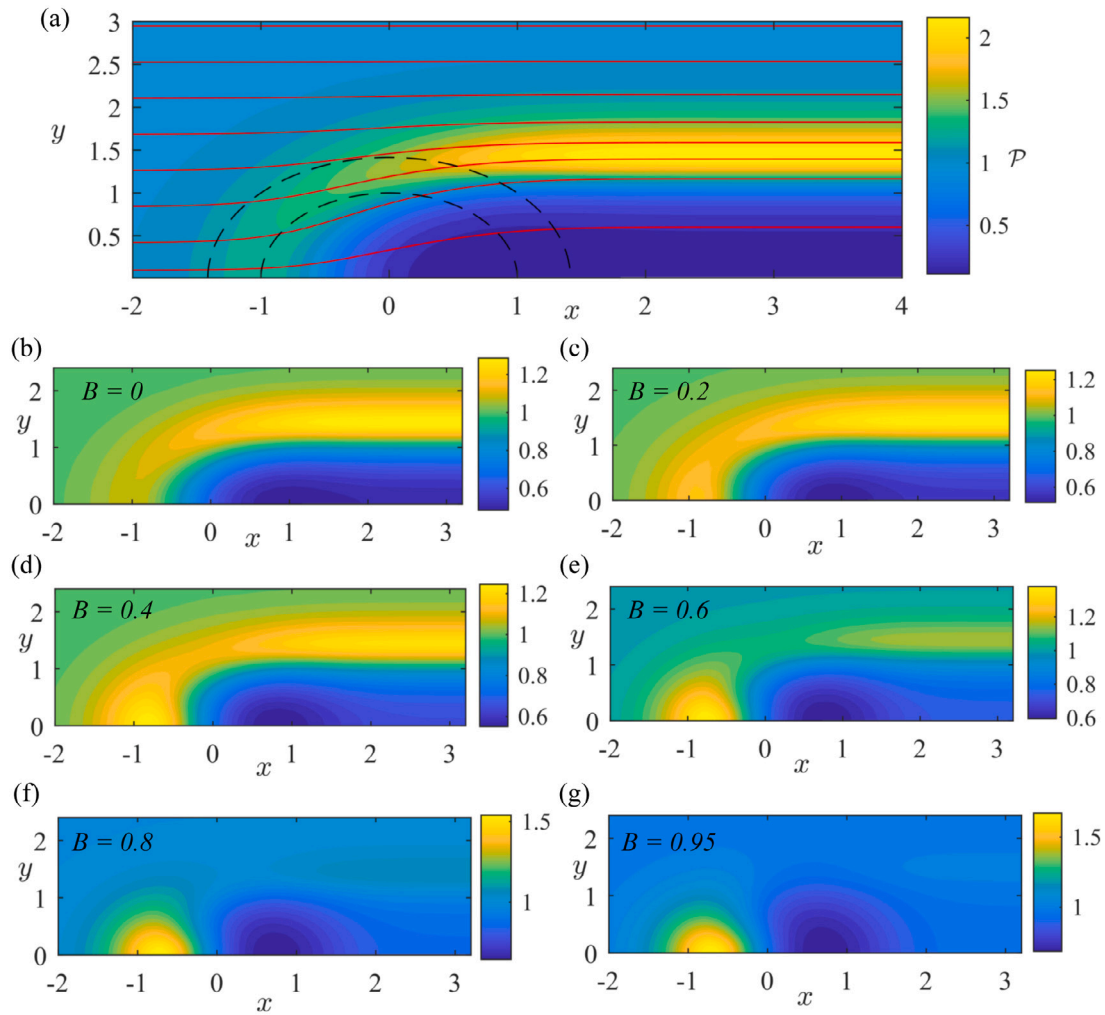


Fig. 6. (a) Colourmap of the relative flux, $\mathcal{P}(x, y)$ for $\mathcal{M} = 0.5$ and the characteristic projections (continuous lines). The dashed lines denote the circles $r = 1$ and $r = \sqrt{2}$. (b–g) Corresponding colourmaps of the flow thickness, h_0 for various values of B .

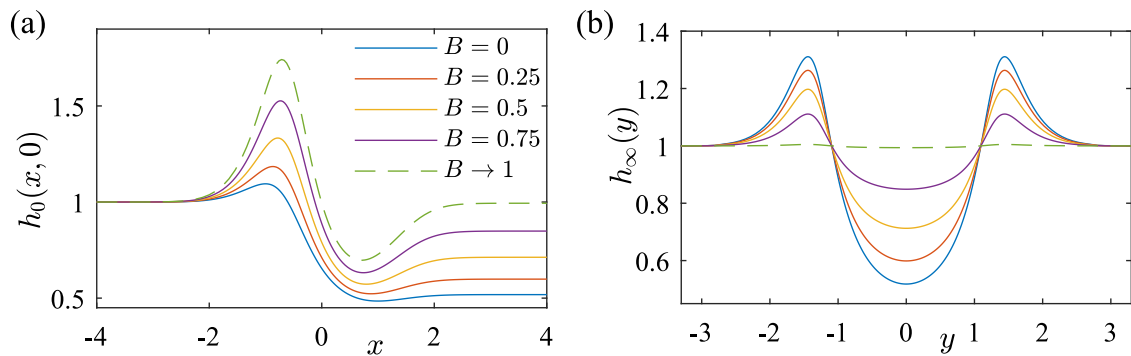


Fig. 7. Flow thickness predicted by the characteristic solution, h_0 , (see Eq. (32)) for the case $\mathcal{M} = 0.5$. (a) Along the centreline, $y = 0$. (b) Cross-section far downstream, $x \rightarrow \infty$.

flow thickness is identical to the case of a laterally extensive mound and they have the same maximum flow thickness, $(1 - \mathcal{M}/\mathcal{M}_c)^{-1}$ (see Section 3). The flow thickness given by (35) arises from maintaining the fake yield surface at exactly $z = 0$ rather than explicitly enforcing mass continuity. This analysis breaks down for uphill mounds ($\mathcal{M} > \mathcal{M}_c$).

When B is close to 1, the flow thickness can be calculated for any value of F by using Charpit’s method to solve the equation $Y = 0$ [35]. Details are given in C. The method is shown to accurately capture the flow thickness for the case $F = 1$ and $\mathcal{M} = 0.3$ in Fig. 9. The solution to $Y = 0$ neglects the cross-stream diffusive slumping, even for $F > 0$.

For larger mounds (and thinner flows), the flow is more significantly diverted by the mound, which means that diffusive slumping plays a key role downstream and hence Charpit’s method becomes invalid; for details, see Appendix C.

4.3. Downstream behaviour

The downstream behaviour of $h_0(x, y)$ predicted by the characteristic solution does not converge to $h = 1$ as $x \rightarrow \infty$ (Fig. 7(b)). The cross-slope slumping terms, $F\partial h/\partial y$ must be reintroduced downstream

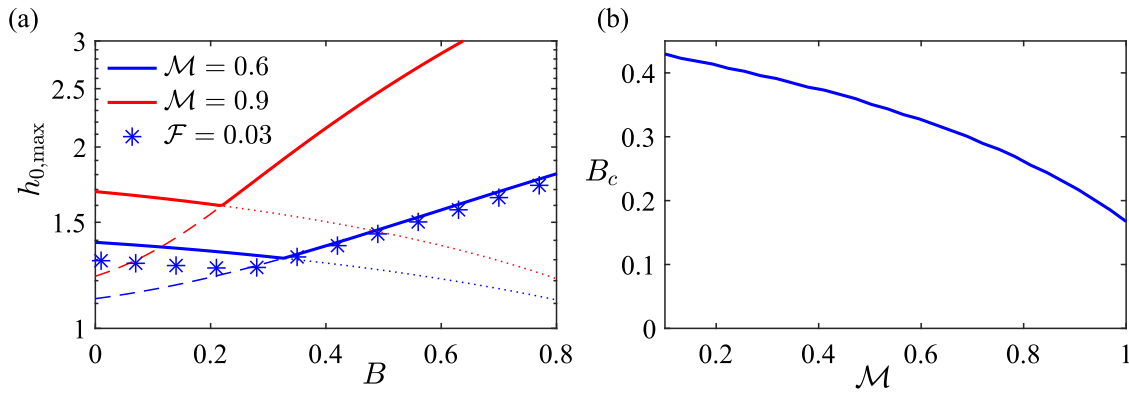


Fig. 8. (a) The maximum flow thickness of the characteristic solution (continuous lines). The upstream local maximum thickness (dashed line) and downstream local maximum (dotted line) are also shown. The blue stars represent the maximum for $\mathcal{F} = 0.03$ and $\mathcal{M} = 0.6$ from the numerical simulations. (b) The critical value of $B = B_c(\mathcal{M})$ at which the global maximum changes location.

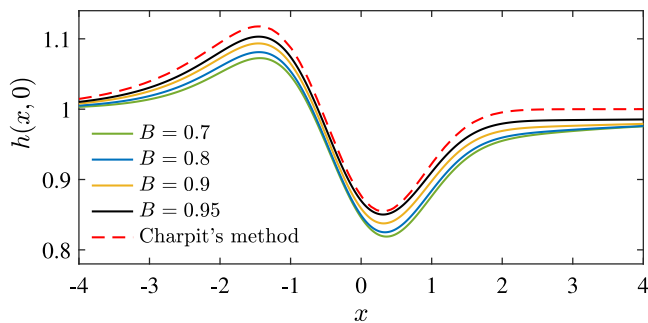


Fig. 9. Flow thickness along the centreline ($y = 0$) for $\mathcal{F} = 1$, $\mathcal{M} = 0.3$ and four values of B . The red dashed line is the prediction from Charpit's method Appendix C.

to capture the redistribution of the flux that was diverted by the mound so that $h \rightarrow 1$ far downstream. To analyse this behaviour in the regime $\mathcal{F} \ll 1$, far downstream of the mound ($x \gg 1$), we write

$$\tilde{x} = \mathcal{F}x. \quad (36)$$

Then

$$\sqrt{(1 - \mathcal{F}h_x - \mathcal{M}m_x)^2 + (\mathcal{F}h_y + \mathcal{M}m_y)^2} = 1 + \dots \quad (37)$$

and hence $Y = h - B$ to leading order. In the present analysis, valid when there are no uphill regions so that the flux is positive everywhere, we have $h > B$. The approximate governing equation becomes

$$\frac{\partial}{\partial \tilde{x}} \left[Y^2(Y + 3B/2) \right] = \frac{\partial}{\partial y} \left[Y^2(Y + 3B/2) \frac{\partial Y}{\partial y} \right]. \quad (38)$$

We integrate Eq. (38) numerically with the initial condition, $Y(\tilde{x} = 0, y) = h_\infty(y) - B$, given by the far-downstream behaviour of the characteristic solution (see Fig. 7(b)). The numerical integration is carried out by discretising the right-hand side using central differences and stepping forward in \tilde{x} using the fourth-order Runge–Kutta method. We recover the thickness via $h = Y + B$. The prediction for h is compared with the numerical result along the centreline in Fig. 10.

5. Isolated topography with an uphill region ($|\mathcal{M}| > \mathcal{M}_c$)

It has previously been shown that in the regime of shallow Newtonian flow ($\mathcal{F} \ll 1$, $B = 0$) past an isolated mound with an uphill region ($\mathcal{M} > \mathcal{M}_c$), there is a dry zone in which there is no fluid [7]. The characteristic projections (32) which were deployed in the previous section to determine the flow thickness for smaller mounds, do not cover the entire plane for $\mathcal{M} > \mathcal{M}_c$ and the flow thickness prediction becomes singular near the edge of the region invaded by the characteristics

owing to the uphill zone where $T_x > 0$. A different approach is needed for these larger mounds. Fig. 11 shows the flow thickness, calculated numerically, in the case that there is an uphill region ($\mathcal{M} = 2$) for a Newtonian fluid (panel a) and a yield-stress fluid with $B = 0.5$ (panel b). Fig. 11(c) shows the height of the 'fake' yield surface, $Y(x, y)$ corresponding to Fig. 11(b); the characteristic projections from (32) are also included in $y \leq 0$. There are numerous interesting features demonstrated in these panels, which we describe in this section.

Some features are reminiscent of the flow over a mound with no uphill region. For example, the variation of the thickness of the Newtonian fluid (Fig. 11(a)) displays some similarities with the yield surface of the Bingham fluid with $B = 0.5$ (Fig. 11(c)). Secondly, the maximum flow thickness occurs along the centreline for the yield-stress fluid whilst for the Newtonian fluid the maximum is cross-slope and further downstream.

The uphill region introduces a major new feature: a dry zone in which there is no fluid. The characteristic projections (Eq. (32)) map out the shape of the upstream edge of the dry zone, which is identical for Newtonian and yield-stress fluids. This suggests that the Newtonian analysis for the behaviour just upstream of the dry zone may be adapted to the case of a yield-stress fluid (see Section 5.1). On the other hand, the downstream shape of the dry zone is different for the Newtonian and yield-stress fluids and there can be different steady solutions for the same parameter values (Fig. 11(b) and Fig. 11(d)); for the latter, we have wetted the region downstream in $r > 2$). This situation is analysed in Section 5.2.

5.1. Upstream edge of the dry zone

Along the centreline, the topography is uphill in $x_1 < x < x_0$ (see Fig. 3). The flow does not surmount the uphill topography. Instead it intrudes slightly beyond $(x, y) = (x_1, 0)$, where $|T_x|$ vanishes. Near this point the flow thickness and its x gradients become large and we write

$$x = x_1 + \mathcal{F}^{1/3}\eta, \quad h = \mathcal{F}^{-1/3}H. \quad (39)$$

Noting that variations of h in the y direction are negligible, we obtain the following second order ordinary differential equation for the flow thickness along the centreline [7],

$$\frac{d}{d\eta} \left(Q \frac{dH}{d\eta} \right) + c_0 \eta \frac{dQ}{d\eta} + c_1 Q = 0, \quad (40)$$

where

$$Q = \left(H - \frac{B}{|dH/d\eta + c_0\eta|} \right)^2 \left(H + \frac{B}{2|dH/d\eta + c_0\eta|} \right) \quad (41)$$

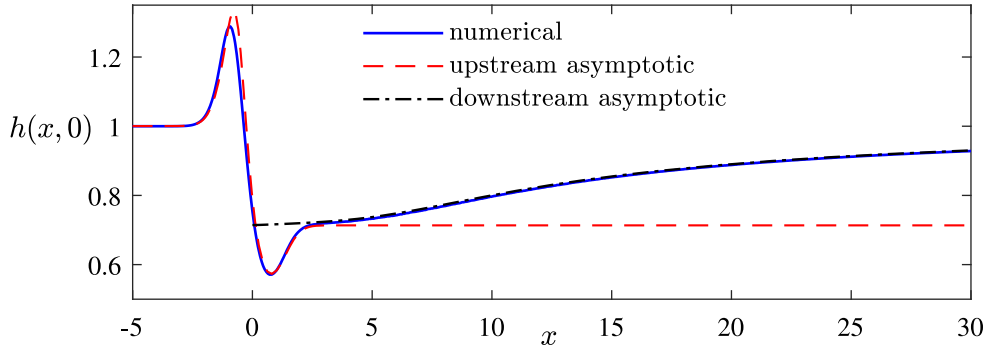


Fig. 10. Flow thickness along the centreline for $B = 0.5$. The numerical result (for $F = 0.1$) is compared to the characteristic ('upstream') asymptotic solution and the 'downstream' prediction of Eq. (38).

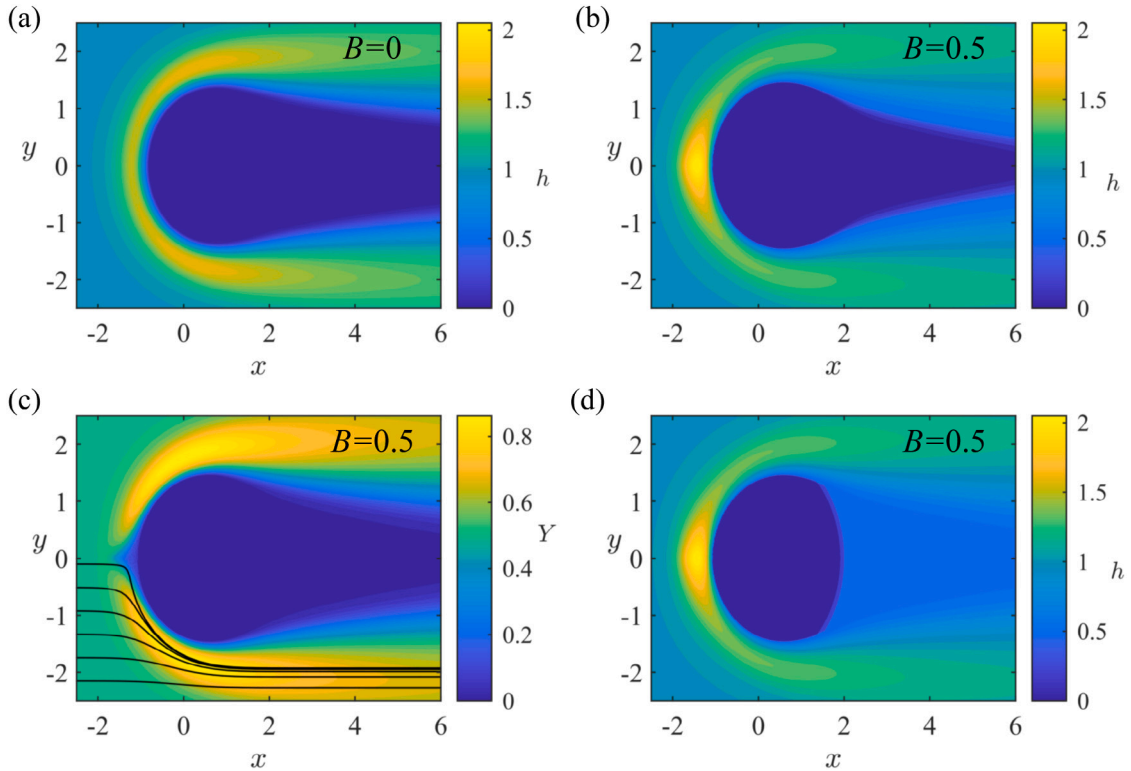


Fig. 11. Flow thicknesses for $\mathcal{M} = 2$ and $F = 0.1$. A dry zone, incorporating the peak of the mound, forms. (a) Flow thickness in the Newtonian case ($B = 0$). (b) Flow thickness for $B = 0.5$. (c) The plug height, Y corresponding to (b). The characteristic projections from (32) are shown in $y < 0$. (d) An alternate steady state for the flow thickness in (b).

and

$$c_0 = \mathcal{M}m_{xx}(x_1, 0), \quad c_1 = \mathcal{M}(\nabla^2 m)(x_1, 0). \quad (42)$$

The first and third terms in Eq. (40) are associated with hydrostatic pressure gradients arising from variations in the flow thickness and the topography, respectively. The topography is locally horizontal at $x = x_1$ (i.e. $\eta = 0$) and the middle term in (40) incorporates gravity acting tangential to the topography. Hence this term changes sign at $\eta = 0$ owing to the change in slope from downhill in $\eta < 0$ to uphill in $\eta > 0$. The behaviour near the contact point ($H \ll 1$) is given by setting $Q = 0$ leading to

$$H \approx \sqrt{2B(\eta_0 - \eta)^{1/2}}, \quad (43)$$

where $\eta = \eta_0$ is the contact point, which is determined as part of the solution. The far-upstream behaviour is given by matching to the characteristic solution for which $h \sim B/|T_x|$ near the uphill region and so

$$H \sim B/c_0|\eta| \quad \text{as } \eta \rightarrow -\infty. \quad (44)$$

We numerically shoot in (40) from $\eta = \eta_0$ and match with the far-field behaviour to obtain $\eta_0 = 0.42$. The solution to (40) is shown to capture well the full numerical result along the centreline for $F = 0.1$, $B = 0.5$, $\mathcal{M} = 2$ in Fig. 12.

We comment that this analysis breaks down for small B in which case different scalings for the flow thickness are needed at $x = x_1$ [7]. For such Newtonian flow, the limiting behaviour of the characteristic solution, h_0 , near the uphill zone is given by mass continuity and depends upon an anomalous exponent of F [7]. In contrast, with a yield-stress fluid, the condition that the yield surface is just above $z = 0$ gives more singular behaviour near the uphill zone and leads to the scaling $h \sim F^{-1/3}$. This difference between Newtonian and yield-stress fluids is another manifestation of what was found in Section 3 when matching to the pond solution for a laterally extensive mound.

5.2. Downstream behaviour

As in the case of shallower topography, the flow is diverted cross-stream by the mound. Further downstream, the flux is redistributed

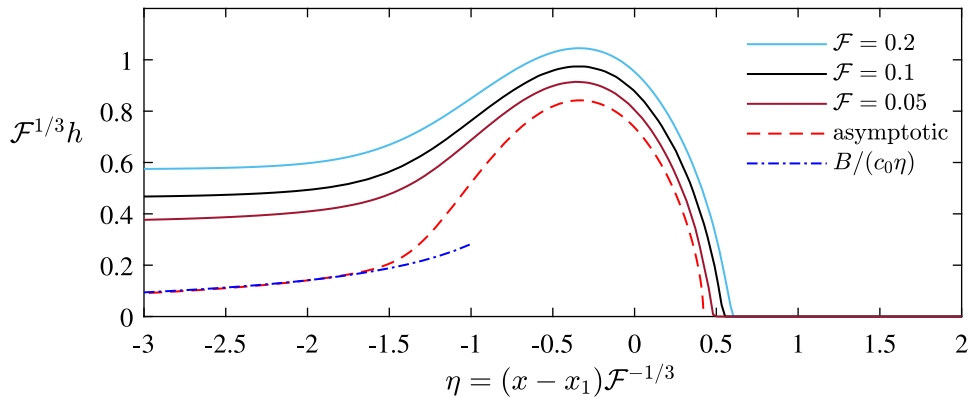


Fig. 12. Flow thickness along the centreline for three values of \mathcal{F} with $B = 0.5$, $\mathcal{M} = 2$ in rescaled coordinates. The asymptotic prediction is given by the solution to (40) with $\eta_0 = 0.42$.

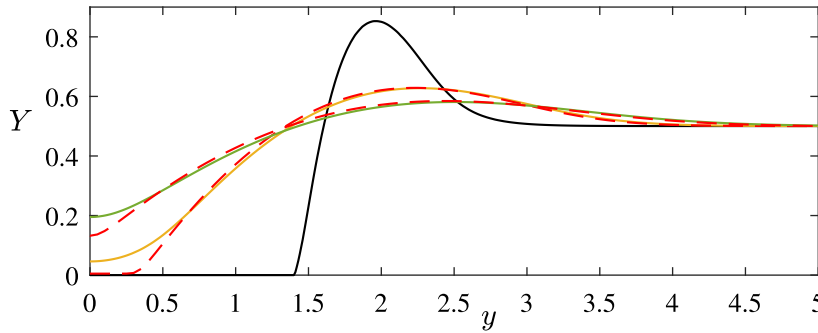


Fig. 13. Cross-sections of the fake yield surface, Y , at $x = 1$ (black line) and $x = 10$ and 20 (solid coloured lines) for $\mathcal{M} = 2$ and $\mathcal{F} = 0.1$. The dashed red lines show the predictions from the asymptotic method of Section 5.2.

by the cross-stream diffusive fluxes so that the free surface returns to its steady constant thickness, $h = 1$. We would like to replicate the downstream analysis of Section 4.3 for the case of an uphill mound but this presents two difficulties. First, for $\mathcal{M} > \mathcal{M}_c$, the method of characteristics does not furnish a sensible downstream solution to use as the initial condition for h ; it has a singularity. Second, the previous downstream analysis required that $h > B$ but there are dry zones ($h = 0$) downstream of larger mounds. To overcome the first issue, we use a cross-section of the numerical solution at $x = 1$ as the initial condition. For the second issue, we solve Eq. (38) for the yield surface Y as before but note that where $Y = 0$, we cannot use the relationship $h = Y + B$ because the material is entirely unyielded and hence the thickness may be less than B . By solving for Y rather than h , we postpone the analysis for $0 < h < B$. The cross-section of Y at $x = 1$ for $\mathcal{M} = 2$ and $\mathcal{F} = 0.1$ is shown as a black line in Fig. 13 and this provides the initial condition for Eq. (38). Cross-sections of the numerical solution further downstream (continuous coloured lines) compare favourably to integrations of (38) (red dashed lines). We can reconstruct the free surface where $Y > 0$ from $h = Y + B > B$.

The flow thickness where $Y = 0$ can be non-unique (see for example Fig. 11(b) and Fig. 11(d)). Far downstream, $|h_x| \ll |h_y|$ and $|m| \ll 1$ so that the flow thickness satisfies

$$h = \frac{B}{\sqrt{1 + (\mathcal{F}h_y)^2}}. \tag{45}$$

One possible solution is $h = B$ in all of the region where $Y = 0$ beyond some downstream edge of the mound at say $r \approx 2$, where there is an adjustment between $h = B$ and $h = 0$ (e.g. Fig. 11(d)). Another possible solution is that there is a small fully unyielded zone at the edge, $y = \pm \bar{y}(x)$, of the yielded flow with free-surface shape

$$y = \pm \bar{y}(x) \mp \mathcal{F} \sqrt{B^2 - h^2}, \tag{46}$$

and beyond this zone the flow thickness vanishes in the interior, $-\bar{y} + \mathcal{F}B < y < \bar{y} - \mathcal{F}B$ (e.g. Fig. 11(b)). Intermediate solutions with $0 < h < B$ within the interior and an adjustment at the edge of the yielding region are also valid. We require additional data to select one of these behaviours.

The zone that is dry or plugged ($Y = 0$) is never invaded by fluid from the line source and so any fully unyielded fluid that was there initially remains there indefinitely. This gives rise to a non-uniqueness when solving for the steady state. We choose the steady state associated with topography that was completely dry prior to the initiation of the line source. There is a fully unyielded region only at the edge of the yielded flow and $h = 0$ beyond this (see Fig. 11(b)) [31]. Details of the adaptations required to the numerical method to obtain this solution are given in Appendix B. However, an example of the non-uniqueness that would arise is that the late-time steady state (in the $Y = 0$ region) following an increase in the line source flux from say $Q/2$ to Q is different to the steady state following a decrease in the flux from $2Q$ to Q . Our results also demonstrate that pre-cursor films, which are sometimes used in transient computations of free-surface viscoplastic flows, may hide dry zones even if the source of the film is subsequently removed because the unyielded material remains covering the zone that may have been dry. This phenomenon does not arise for a Newtonian fluid because pre-existing fluid slowly flows away.

6. Discussion and conclusion

In this paper we have analysed the interaction of a steady free-surface yield stress flow with a topographical feature and compared the results to the case of a viscous Newtonian flow. The flow thickens on shallower slopes and thins on steeper slopes, which is associated with the maintenance of a streamwise volume flux. This response is enhanced at higher yield stresses. For an isolated mound, the flow is

also diverted cross-stream. For the same flow thickness, less fluid is diverted at higher yield stresses because the steady flux is smaller. Hence the thickening of the flow cross-stream is reduced with increasing yield stress. The thickening of the flow upstream is also increased with yield stress owing to the response to a shallower slope. The culmination of these two effects is that the maximum thickness occurs cross-stream and downstream of the mound at low yield stresses but upstream of the mound at higher yield stresses.

In the case that the mound has an uphill region, the flow either develops a thick ponded region to surmount the topography or the flow is entirely diverted around the mound and a dry zone forms. Which of the regimes occurs will depend on the cross-slope dimension of the mound. For a yield-stress fluid, the shape of the dry zone is not unique for a given steady flow; it also depends on the transient evolution as the dry zone may have been previously covered by a slump of plugged fluid that remains stationary.

In many applications, the free surface of the fluid is known but the underlying topography or the rheology is unknown (e.g. glaciers and lava flows) [47]. [48] showed that the method of characteristics can be used to reconstruct the topography required to produce a particular free-surface profile for a thin Newtonian. In the case of lava flows, the topography is typically known prior to the emplacement but the rheology is highly uncertain. Our results provide a first step towards developing an inverse method for constraining rheology from the topography and the free surface. We have shown that lavas with higher yield stresses are likely have their maximum thicknesses upstream of obstructions whilst the maximum thickness arises from diversion cross-stream for those with lower yield stresses.

Another important avenue of further research is to analyse carefully the transient evolution to the steady flow. There has been some success in accurately predicting the paths of lava flows but estimating the temporal evolution and inundation timing have been very challenging [21,49]. In the problem considered in this paper, the characteristics that described flow around an isolated mound may be extended to incorporate a time derivative. The downstream re-joining of the flow owing to cross-stream diffusive fluxes is a very slow process owing to the relatively small thickness of the current and consequently, the convergence to the steady upstream maximum thickness is much faster than the evolution to the final dry zone shape.

Finally, it would be interesting to incorporate inertia into the problem and analyse how this affects the surmounting of uphill mounds as has been studied for Newtonian flows [50]. Such investigation may also assist in developing models for granular flows around topography; for example the case of a laterally extensive mound is sensitive to any stationary deposited material prior to initiation of the current [51].

Declaration of competing interest

The authors declare that they have no known competing financial interests or personal relationships that could have appeared to influence the work reported in this paper.

Acknowledgements

E.M.H. is grateful to the School of Mathematics and Statistics, The University of Melbourne, Australia for the award of a Harcourt-Doig research fellowship.

Appendix A. Matching to the pond

We match the pond solution (22), valid in $x_2 < x < x_0$, to $h_0(x)$ at $x = x_0$. Near, but just downstream of x_0 , we have $|T_x| \ll 1$ and the behaviour of h_0 and h_1 here is given by (Eqs. (15) and (16)),

$$h_0 \sim \frac{B}{|T_x|} + \left(\frac{2(1-B)^2(1+B/2)}{3B} \right)^{1/2}, \quad h_1 \sim \frac{B^2 \mathcal{M}m''(x)}{|T_x|^4}. \quad (\text{A.1})$$

This behaviour differs from the Newtonian case ($B = 0$) for which $h_0 \sim |T_x|^{-1/3}$ and $h_1 \sim |T_x|^{-8/3}$ near x_0 . The scalings for the Newtonian case arise from imposing that the flux is constant as x_0 is approached from downstream. However, for $B > 0$, we require that the fluid does not fully plug over its thickness ($Y > 0$) as x_0 is approached, which requires more extreme behaviour than the flux condition and imposes $h_0 \sim |T_x|^{-1}$. These two different limiting behaviours near the uphill region for the Newtonian and yield-stress fluids will lead to different magnitudes for γ , which determines the scale of the perturbation to the horizontal static layer within the pond region (see (22)).

To match the pond and order unity expansions for a yield-stress fluid, we introduce an intermediate region and write

$$x = x_0 + \mathcal{F}^{1/3} B^{1/3} \chi^{-2/3} \eta, \quad h = \mathcal{F}^{-1/3} B^{2/3} \chi^{-1/3} H, \quad (\text{A.2})$$

where the scalings are chosen for a balance in the first two terms of the outer $h \sim 1$ expansion (A.1) and we have introduced

$$\chi = -\mathcal{M}m''(x_0). \quad (\text{A.3})$$

The leading order equation (from (11)) in the intermediate region is

$$\frac{dH}{d\eta} + \frac{1}{H} = \eta, \quad (\text{A.4})$$

which is equivalent to requiring that the flow is fully plugged, $Y = 0$, at leading order. This equation has the following exact implicit solution

$$\eta = -2^{2/3} \frac{Ai'[(\eta^2/2 - H)/2^{1/3}]}{Ai[(\eta^2/2 - H)/2^{1/3}]} \quad (\text{A.5})$$

where Ai is the Airy function. The behaviour up and downstream is given by matching to the respective expansions;

$$H \sim \eta^2/2 + c_0 \quad \eta \rightarrow -\infty, \quad (\text{A.6})$$

$$H \sim \eta^{-1} - \eta^{-4} \quad \eta \rightarrow +\infty. \quad (\text{A.7})$$

We also obtain

$$c_{-1} = -x_0 + \mathcal{M}m(x_0), \quad \gamma = \mathcal{F}^{-1/3} \chi^{-1/3} B^{2/3}, \quad (\text{A.8})$$

from matching with the pond. As $\eta \rightarrow -\infty$, the right-hand side of (A.5) becomes singular, in order to satisfy (A.6). This corresponds to the first zero of the Airy function from which we obtain,

$$c_0 = 2.946 \quad \text{to 3 decimal places.} \quad (\text{A.9})$$

This fully determines the first two terms in the pond expansion. There is also a relatively unimportant matching region at $x = x_2$; for details of an analogous procedure for a Newtonian fluid, see [7].

Appendix B. Numerical integration for an isolated feature

We first describe the numerical approach in the case that there is no dry zone ($\mathcal{M} < \mathcal{M}_c$, Section 4), which follows the approach of [52]. To solve the steady problem, $\nabla \cdot \mathbf{q} = 0$, we recast it in weak form by multiplying by a test function v and integrating by parts over the domain, Ω to obtain

$$\int \int_{\Omega} \mathbf{q} \cdot \nabla v \, dx dy = 0, \quad (\text{B.1})$$

where $\Omega = [-a, b] \times [-c, c]$ is a rectangle and we have applied the boundary condition $h = 1$ on its boundaries, which corresponds to $v = 0$. This variational problem is solved in FEniCS via a finite-element method [53]. The steady solution is found by initially guessing that $h = 1$ everywhere and iterating until a converged solution that accounts for the topography is obtained. The domain size is chosen so that increases to its size lead to negligible changes in the solution. For $\mathcal{M} < \mathcal{M}_c$, the flow thickness, h , and fake yield surface, Y are positive everywhere and the method obtains a converged solution (e.g. Fig. 5). To verify the numerical results, the maximum thickness obtained for

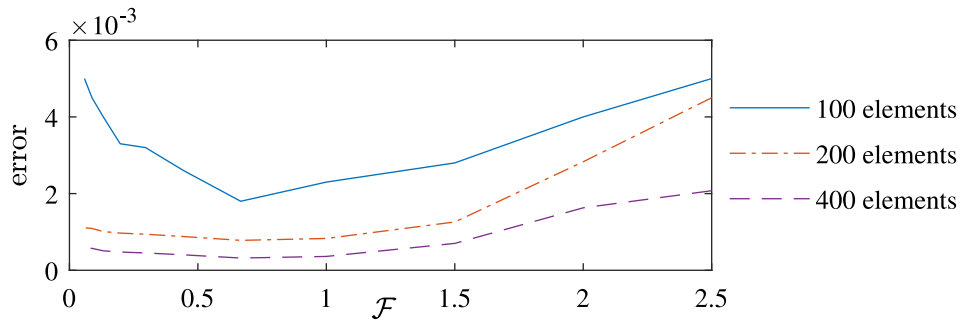


Fig. B.14. Relative error for the FEniCS numerical prediction for the maximum flow thickness for a laterally extensive mound with $B = 0.4$ and $\mathcal{M} = 0.5$ as compared to the one-dimensional integration. The number of elements per unit square is shown.

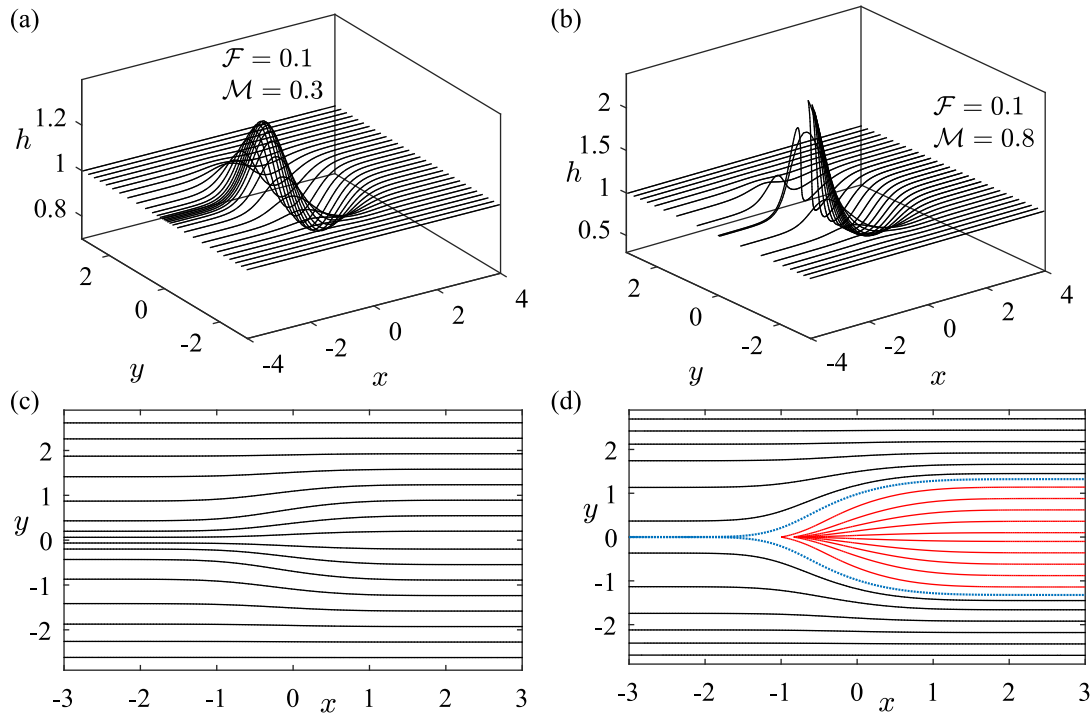


Fig. C.15. (a, b) Flow thickness for $B = 1$ with $h \rightarrow 1$ as $r \rightarrow \infty$. (c, d) Corresponding characteristic projections. The red lines show the characteristics that meet the seam and the dotted blue line represents the limiting characteristic emanating from $y = 0$ upstream.

a laterally extensive mound from FEniCS was compared to the one-dimensional integration in Section 3. The relative error for 100, 200 and 400 elements per unit square is shown in Fig. B.14 in the case that $B = 0.4$ and $\mathcal{M} = 0.5$. For the figures in this paper, we typically used 2000 elements per unit square.

In the case that there is a dry region (Section 5), an adjusted approach is needed owing to the degeneracy as $h \rightarrow 0$. First, we obtain a prediction for the shape of the dry region from the method of characteristics (32); the region not accessed by the characteristics is an outer bound on the dry region. For a Newtonian fluid ($B = 0$), we ensure that $h > 0$ by adding a small flux over the dry region and the governing equation becomes $\nabla \cdot \mathbf{q} = \epsilon(x, y)$ [7]. We set $\epsilon = \epsilon_0$ in the region bounded by the limiting characteristics and the line $x = 10$ (see Fig. 11(c)) and $\epsilon = 0$ elsewhere. We use $\epsilon_0 = 10^{-5}$. The solution can then be obtained as before and the dry zone is covered by a very thin film of fluid.

In the case that yield stresses are important ($B > 0$), this method needs further adaptation because the introduction of a small additional flux over the dry zone will lead to $Y \ll 1$, rather than $h \ll 1$, and thus h may be of order B in the supposedly dry zone (see Section 5.2). To overcome this difficulty, we regularise the stress-strain relationship

following the appendix of [9] so that h is small when the flux is small. In the flux q , we replace Y with

$$\frac{1}{2} \left[Y + \sqrt{Y^2 + \frac{\nu h^{3/2}}{B[(1 - Fh_x - \mathcal{M}m_x)^2 + (Fh_y + \mathcal{M}m_y)^2 + \nu^2]}} \right], \quad (\text{B.2})$$

where ν is a regularisation parameter, which we typically take to be $\nu = 10^{-4}$. The system can then be solved in FEniCS noting that the steady solution obtained corresponds to the scenario in which the dry zone was never invaded by fluid. If the dry region was invaded by the fluid prior to the initiation of the upstream line source, then a different steady late-time solution is required as discussed in Section 5. This non-uniqueness does not occur for a Newtonian fluid.

Appendix C. Charpit's method for the flow thickness ($B \approx 1$)

In the limiting regime of a very high yield stress, the governing equation may be approximated by $Y = 0$ with boundary condition $h \rightarrow 1$ in the far field. For any $F > 0$, the equation $Y = 0$ (Eq. (6)) may be solved by applying Charpit's method, which yields the following characteristic equations [see chapter 8 of 54]

$$\dot{x} = 2F(1 - Fp - \mathcal{M}m_x) \quad (\text{C.1})$$

$$\dot{y} = -2F(Fq + \mathcal{M}m_y) \quad (\text{C.2})$$

$$\dot{p} = -2\mathcal{M}m_{xx}(1 - Fp - \mathcal{M}m_x) - 2\mathcal{M}m_{xy}(Fq + \mathcal{M}m_y) + 2pB^2/h^3 \quad (\text{C.3})$$

$$\dot{q} = -2\mathcal{M}m_{xy}(1 - Fp - \mathcal{M}m_x) - 2\mathcal{M}m_{yy}(Fq + \mathcal{M}m_y) + 2qB^2/h^3 \quad (\text{C.4})$$

$$\dot{h} = 2Fp(1 - Fp - \mathcal{M}m_x) - 2Fq(Fq + \mathcal{M}m_y) \quad (\text{C.5})$$

where $p = \partial h / \partial x$ and $q = \partial h / \partial y$ and the dot denotes the derivative in the direction of the characteristics. These equations are integrated in the negative x direction from $x = +\infty$ with boundary condition $h = 1$ since a numerical instability arises when integrating in the positive x direction. The solution and characteristic projections in the (x, y) -plane are shown in Fig. C.15 for $F = 0.1$. Fig. C.15 shows that the characteristics may cross (red lines), even for mounds with no uphill region ($\mathcal{M} < \mathcal{M}_c$). To avoid intersecting characteristics, we introduce a seam by terminating the characteristics at $y = 0$ to maintain a continuous single-valued free surface [35]. We note that as a consequence $\partial h / \partial y$ is not necessarily zero along the centreline. Charpit's method may be applied to obtain profiles that satisfy $Y = 0$ and $h \rightarrow 1$ in the far-field even for $\mathcal{M} > \mathcal{M}_c$ by introducing a seam.

In the case that the characteristics do not cross, Charpit's method provides the limiting thickness for steady flow over a mound at very high yield stresses (since $Y \rightarrow 0$ as $B \rightarrow 1$). However, in the case that the characteristics cross, the mathematical solution to the problem $Y = 0$, $h \rightarrow 1$ in the far-field may not be the correct solution for the steady flow thickness. The mathematical solution corresponds to a plugged lump of fluid that is stationary everywhere. The entropy condition is violated because data is required to leave the seam and travel downstream (red lines in Fig. C.15(d)), which is unphysical if the fluid is flowing slowly downslope. There is a limiting characteristic which bounds the area that is physically accessed by the characteristics emanating from upslope (blue dashed line in Fig. C.15(d)). To mathematically capture the fluid that flows from upstream into the zone bounded by the blue dashed line requires the reintroduction of non-negligible flux. Indeed, the solution to $Y = 0$ cannot capture the restriction that thin flows cannot surmount uphill topography unless they deepen.

References

- [1] L.E. Stillwagon, R.G. Larson, Leveling of thin films over uneven substrates during spin coating, *Phys. Fluids A* 2 (11) (1990) 1937–1944, <http://dx.doi.org/10.1063/1.857669>.
- [2] M.M.J. Décré, J.-C. Baret, Gravity-driven flows of viscous liquids over two-dimensional topographies, *J. Fluid Mech.* 487 (2003) 147–166, <http://dx.doi.org/10.1017/S0022112003004774>.
- [3] S. Kalliadasis, C. Bielarz, G.M. Homsy, Steady free-surface thin film flows over topography, *Phys. Fluids* 12 (8) (2000) 1889–1898, <http://dx.doi.org/10.1063/1.870438>.
- [4] P.H. Gaskell, P.K. Jimack, M. Sellier, H.M. Thompson, M.C.T. Wilson, Gravity-driven flow of continuous thin liquid films on non-porous substrates with topography, *J. Fluid Mech.* 509 (2004) 253–280, <http://dx.doi.org/10.1017/S0022112004009425>.
- [5] D. Takagi, H.E. Huppert, The effect of confining boundaries on viscous gravity currents, *J. Fluid Mech.* 577 (2007) 495–505, <http://dx.doi.org/10.1017/S0022112007005174>.
- [6] N. Aksel, M. Schörner, Films over topography: from creeping flow to linear stability, theory, and experiments, a review, *Acta Mech.* 229 (4) (2018) 1453–1482, <http://dx.doi.org/10.1007/s00707-018-2146-y>.
- [7] E.M. Hinton, A.J. Hogg, H.E. Huppert, Interaction of viscous free-surface flows with topography, *J. Fluid Mech.* 876 (2019) 912–938, <http://dx.doi.org/10.1017/jfm.2019.588>.
- [8] R.M. Iverson, The physics of debris flows, *Rev. Geophys.* 35 (3) (1997) 245–296, <http://dx.doi.org/10.1029/97RG00426>.
- [9] N.J. Balmforth, A.S. Burbidge, R.V. Craster, J. Salzig, A. Shen, Visco-plastic models of isothermal lava domes, *J. Fluid Mech.* 403 (2000) 37–65, <http://dx.doi.org/10.1017/S0022112099006916>.
- [10] R.C. Kerr, R.W. Griffiths, K.V. Cashman, Formation of channelized lava flows on an unconfined slope, *J. Geophys. Res.: Solid Earth* 111 (B10) (2006) <http://dx.doi.org/10.1029/2005JF004225>.
- [11] C. Ancey, Plasticity and geophysical flows: a review, *J. Non-Newton. Fluid Mech.* 142 (1–3) (2007) 4–35, <http://dx.doi.org/10.1016/j.jnnfm.2006.05.005>.
- [12] H.R. Dieterich, K.V. Cashman, Channel networks within lava flows: Formation, evolution, and implications for flow behavior, *J. Geophys. Res.: Earth Surface* 119 (8) (2014) 1704–1724, <http://dx.doi.org/10.1002/2014JF003103>.
- [13] H.R. Dieterich, E. Lev, J. Chen, J.A. Richardson, K.V. Cashman, Benchmarking computational fluid dynamics models of lava flow simulation for hazard assessment, forecasting, and risk management, *J. Appl. Volcanol.* 6 (1) (2017) 1–14, <http://dx.doi.org/10.1186/s13617-017-0061-x>.
- [14] F. Deng, M. Rodgers, S. Xie, T.H. Dixon, S. Charbonnier, E.A. Gallant, C.M.L. Vélez, M. Ordoñez, R. Malservisi, N.K. Voss, et al., High-resolution DEM generation from spaceborne and terrestrial remote sensing data for improved volcano hazard assessment—A case study at nevado del ruiz, Colombia, *Remote Sens. Environ.* 233 (2019) 111348, <http://dx.doi.org/10.1016/j.rse.2019.111348>.
- [15] A.R. Darnell, J.C. Phillips, J. Barclay, R.A. Herd, A.A. Lovett, P.D. Cole, Developing a simplified geographical information system approach to dilute lahar modelling for rapid hazard assessment, *Bull. Volcanol.* 75 (4) (2013) 1–16, <http://dx.doi.org/10.1007/s00445-013-0713-6>.
- [16] X. Cui, H. Jeffrey, J.S. Greenbaum, J. Guo, L. Li, L.E. Lindzey, F.A. Habbal, W. Wei, D.A. Young, N. Ross, et al., Bed topography of princess elizabeth land in east antarctica, *Earth Syst. Sci. Data* 12 (4) (2020) 2765–2774, <http://dx.doi.org/10.5194/essd-12-2765-2020>.
- [17] E. Gallant, J. Richardson, C. Connor, P. Wetmore, L. Connor, A new approach to probabilistic lava flow hazard assessments, applied to the Idaho National Laboratory, eastern snake river plain, Idaho, USA, *Geology* 46 (10) (2018) 895–898, <http://dx.doi.org/10.1130/G45123.1>.
- [18] J.P. Lockwood, F.A. Torgerson, Diversion of lava flows by aerial bombing—lessons from mauna loa volcano, hawaii, *Bull. Volcanol.* 43 (4) (1980) 727–741, <http://dx.doi.org/10.1007/BF02600367>.
- [19] S. Scifoni, M. Coltelli, M. Marsella, C. Proietti, Q. Napoleoni, A. Vicari, C. Del Negro, Mitigation of lava flow invasion hazard through optimized barrier configuration aided by numerical simulation: The case of the 2001 etna eruption, *J. Volcanol. Geotherm. Res.* 192 (1–2) (2010) 16–26, <http://dx.doi.org/10.1016/j.jvolgeores.2010.02.002>.
- [20] C. Del Negro, L. Fortuna, A. Herault, A. Vicari, Simulations of the 2004 lava flow at Etna volcano using the magflow cellular automata model, *Bull. Volcanol.* 70 (7) (2008) 805–812, <http://dx.doi.org/10.1007/s00445-007-0168-8>.
- [21] A.J. Harris, S.K. Rowland, FLOWGO 2012, An Updated Framework for Thermorheological Simulations of Channel-Contained Lava, in: *Hawaiian Volcanoes: From Source To Surface*, Geophysical Monograph Series, vol. 208, 2015, pp. 457–481.
- [22] P.C. Smith, A similarity solution for slow viscous flow down an inclined plane, *J. Fluid Mech.* 58 (2) (1973) 275–288, <http://dx.doi.org/10.1017/S0022112073002594>.
- [23] J.R. Lister, Viscous flows down an inclined plane from point and line sources, *J. Fluid Mech.* 242 (1992) 631–653, <http://dx.doi.org/10.1017/S0022112092002520>.
- [24] G.I. Taylor, D.H. Michael, On making holes in a sheet of fluid, *J. Fluid Mech.* 58 (4) (1973) 625–639, <http://dx.doi.org/10.1017/S0022112073002375>.
- [25] S.K. Wilson, B.R. Duffy, S.H. Davis, On a slender dry patch in a liquid film draining under gravity down an inclined plane, *European J. Appl. Math.* 12 (3) (2001) 233–252, <http://dx.doi.org/10.1017/S095679250100417X>.
- [26] A. Mazouchi, G.M. Homsy, Free surface Stokes flow over topography, *Phys. Fluids* 13 (10) (2001) 2751–2761, <http://dx.doi.org/10.1063/1.1401812>.
- [27] M. Sellier, Y.C. Lee, H.M. Thompson, P.H. Gaskell, Thin film flow on surfaces containing arbitrary occlusions, *Comput. & Fluids* 38 (1) (2009) 171–182, <http://dx.doi.org/10.1016/j.compfluid.2008.01.008>.
- [28] M. Sellier, Modelling the wetting of a solid occlusion by a liquid film, *Int. J. Multiph. Flow.* 71 (2015) 66–73, <http://dx.doi.org/10.1016/j.ijmultiphaseflow.2014.12.007>.
- [29] E.M. Hinton, A.J. Hogg, H.E. Huppert, Viscous free-surface flows past cylinders, *Phys. Rev. Fluids* 5 (8) (2020) 084101, <http://dx.doi.org/10.1103/PhysRevFluids.5.084101>.
- [30] E.M. Hinton, A.J. Hogg, H.E. Huppert, Shallow free-surface Stokes flow around a corner, *Phil. Trans. R. Soc. A* 378 (2174) (2020) 20190515, <http://dx.doi.org/10.1098/rsta.2019.0515>.
- [31] P. Coussot, S. Proust, Slow, unconfined spreading of a mudflow, *J. Geophys. Res.: Solid Earth* 101 (B11) (1996) 25217–25229, <http://dx.doi.org/10.1029/96JB02486>.
- [32] D.R. Hewitt, N.J. Balmforth, Thixotropic gravity currents, *J. Fluid Mech.* 727 (2013) 56–82, <http://dx.doi.org/10.1017/JFM.2013.235>.
- [33] K.F. Liu, C.C. Mei, Slow spreading of a sheet of bingham fluid on an inclined plane, *J. Fluid Mech.* 207 (1989) 505–529, <http://dx.doi.org/10.1017/S0022112089002685>.
- [34] N.J. Balmforth, R.V. Craster, A consistent thin-layer theory for Bingham plastics, *J. Non-Newton. Fluid Mech.* 84 (1) (1999) 65–81, [http://dx.doi.org/10.1016/S0377-0257\(98\)00133-5](http://dx.doi.org/10.1016/S0377-0257(98)00133-5).
- [35] N.J. Balmforth, R.V. Craster, R. Sassi, Shallow viscoplastic flow on an inclined plane, *J. Fluid Mech.* 470 (2002) 1–29, <http://dx.doi.org/10.1017/S0022112002001660>.
- [36] N. Dubash, N.J. Balmforth, A.C. Slim, S. Cochard, What is the final shape of a viscoplastic slump? *J. Non-Newton. Fluid Mech.* 158 (1–3) (2009) 91–100, <http://dx.doi.org/10.1016/j.jnnfm.2008.08.004>.
- [37] C. Ancey, S. Cochard, The dam-break problem for herschel-bulkley viscoplastic fluids down steep flumes, *J. Non-Newton. Fluid Mech.* 158 (1–3) (2009) 18–35, <http://dx.doi.org/10.1016/j.jnnfm.2008.08.008>.

- [38] A.J. Hogg, G.P. Matson, Slumps of viscoplastic fluids on slopes, *J. Non-Newton. Fluid Mech.* 158 (1–3) (2009) 101–112, <http://dx.doi.org/10.1016/j.jnnfm.2008.07.003>.
- [39] N.J. Balmforth, R.V. Craster, A.C. Rust, R. Sassi, Viscoplastic flow over an inclined surface, *J. Non-Newton. Fluid Mech.* 139 (1–2) (2006) 103–127, <http://dx.doi.org/10.1016/j.jnnfm.2006.07.010>.
- [40] I.R. Ionescu, Viscoplastic shallow flow equations with topography, *J. Non-Newton. Fluid Mech.* 193 (2013) 116–128, <http://dx.doi.org/10.1016/j.jnnfm.2012.09.009>.
- [41] C.C. Mei, M. Yuhi, Slow flow of a Bingham fluid in a shallow channel of finite width, *J. Fluid Mech.* 431 (2001) 135–159, <http://dx.doi.org/10.1017/S0022112000003013>.
- [42] S.K. Wilson, B.R. Duffy, A.B. Ross, On the gravity-driven draining of a rivulet of a viscoplastic material down a slowly varying substrate, *Phys. Fluids* 14 (2) (2002) 555–571, <http://dx.doi.org/10.1063/1.1416882>.
- [43] M. Yuhi, C.C. Mei, Slow spreading of fluid mud over a conical surface, *J. Fluid Mech.* 519 (2004) 337–358, <http://dx.doi.org/10.1017/S0022112004001478>.
- [44] C.C. Mei, K.-F. Liu, M. Yuhi, *Mud flow—slow and fast*, in: *Geomorphological Fluid Mechanics*, Springer, 2001, pp. 548–577.
- [45] E.C. Bingham, *Fluidity and Plasticity*, McGraw-Hill, 1922.
- [46] S.K. Wilson, R. Hunt, B.R. Duffy, On the critical solutions in coating and rimming flow on a uniformly rotating horizontal cylinder, *Quart. J. Mech. Appl. Math.* 55 (3) (2002) 357–383, <http://dx.doi.org/10.1093/qjmam/55.3.357>.
- [47] C. Heining, M. Sellier, N. Aksel, The inverse problem in creeping film flows, *Acta Mech.* 223 (4) (2012) 841–847, <http://dx.doi.org/10.1007/s00707-011-0599-3>.
- [48] M. Sellier, S. Panda, Beating capillarity in thin film flows, *Internat. J. Numer. Methods Fluids* 63 (4) (2010) 431–448, <http://dx.doi.org/10.1002/flid.2086>.
- [49] M.P. Poland, T.R. Orr, J.P. Kauahikaua, S.R. Brantley, J.L. Babb, M.R. Patrick, C.A. Neal, K.R. Anderson, L. Antolik, M. Burgess, et al., The 2014–2015 Pāhoa lava flow crisis at Kīlauea volcano, Hawai‘i: Disaster avoided and lessons learned, *GSA Today* 26 (2) (2016) 4–10, <http://dx.doi.org/10.1130/GSATG262A.1>.
- [50] S. Veremieiev, H.M. Thompson, Y.C. Lee, P.H. Gaskell, Inertial thin film flow on planar surfaces featuring topography, *Comput. & Fluids* 39 (3) (2010) 431–450, <http://dx.doi.org/10.1016/j.compfluid.2009.09.007>.
- [51] S. Viroulet, J.L. Baker, A.N. Edwards, C.G. Johnson, C. Gjaltema, P. Clavel, J.M.N.T. Gray, Multiple solutions for granular flow over a smooth two-dimensional bump, *J. Fluid Mech.* 815 (2017) 77–116, <http://dx.doi.org/10.1017/jfm.2017.41>.
- [52] E.M. Hinton, A.J. Hogg, Modelling the influence of a variable permeability inclusion on free-surface flow in an inclined aquifer, *Water Resour. Res.* 57 (4) (2021) e2020WR029195, <http://dx.doi.org/10.1029/2020WR029195>.
- [53] H.P. Langtangen, A. Logg, *Solving PDEs in Python: The FEniCS Tutorial I*, Springer Nature, 2016.
- [54] J.R. Ockendon, S. Howison, A. Lacey, A. Movchan, *Applied partial differential equations*, Oxford University Press, 2003.